The globus pallidus orchestrates abnormal network dynamics in a model of Parkinsonism

Brice de La Crompe, Asier Aristieta, Arthur Leblois, Salma Elsherbiny, Thomas Boraud, Nicolas Mallet

The globus pallidus orchestrates abnormal network dynamics in Parkinsonism

Authors: Brice de la Crompe[1,2], Asier Aristieta[1,2], Arthur Leblois[1,2], Salma Elsherbiny[1,2], Thomas Boraud[1,2], Nicolas P. Mallet [1,2*]

Affiliations:

[1] Université de Bordeaux, Institut des Maladies Neurodégénératives, Bordeaux, France.
[2] CNRS UMR 5293, Institut des Maladies Neurodégénératives, 33076 Bordeaux, France.

[*]Correspondence should be addressed to nicolas.mallet@u-bordeaux.fr

Keywords: *basal ganglia, abnormal network dynamics, Parkinson's disease, beta oscillations, optogenetic manipulation, motor cortex, subthalamic nucleus, globus pallidus.*

Abstract

The dynamical properties of cortico-basal ganglia (CBG) circuits are dramatically altered following the loss of dopamine in Parkinson's disease (PD). The neural circuit dysfunctions associated with PD include spike-rate alteration concomitant with excessive oscillatory spike-synchronization in the beta frequency range (12-30 Hz). Which neuronal circuits orchestrate and propagate these abnormal neural dynamics in CBG remains unknown. In this work, we combined *in vivo* electrophysiological recordings with advanced optogenetic manipulations in normal and 6-OHDA rats to shed light on the mechanistic principle underlying circuit dysfunction in PD. Our results show that abnormal neural dynamics present in a rat model of PD do not rely on cortical or subthalamic nucleus activity but critically dependent on globus pallidus (GP) integrity. Our findings highlight the pivotal role played by the GP which operates as a hub nucleus capable of orchestrating firing rate and synchronization changes across CBG circuits both in normal and pathological conditions.

Introduction

Normal brain functions rely on the overall modulation of cell firing activity and the precise control over the spatiotemporal firing pattern, including (possibly synchronized) oscillatory activity among neuronal network and brain areas [1,2]. Disruption in the dynamical properties orchestrating local firing rates and global network oscillations changes are observed in many neurological disorders [3]. This is particularly well-illustrated in the basal ganglia (BG) where the loss of dopamine in Parkinson's disease (PD) is associated with persistent alterations in both the firing rate [4,5] and oscillatory synchronization among and between BG nuclei [6–8]. Defining how these changes interact and are orchestrated is a key aspect to better understand the circuit mechanism underlying their generation.

On one hand, spike-rate changes are the backbone of the classic model of BG dysfunction [9]. In this scheme, dopaminergic loss in the striatum triggers an imbalance in the firing activity of striatal neurons involved in BG direct and indirect pathways, resulting in a cascade of firing rate changes along these circuits which ultimately leads to an over-inhibition of the motor system [4,5]. The direct/indirect striatal imbalance in firing activity has been confirmed experimentally [10,11], and the effect of firing rate alterations on the motor deficits in PD is highlighted by optogenetic studies showing that driving hyperactivity in indirect pathway striatal neurons generates a parkinsonian-like state in rodent [12]. In addition, spike-rate features can be predicative of parkinsonism [13,14].

On the other hand, changes in BG oscillatory activity are also recognized as a critical functional change associated with PD [15]. It materializes as an excessive expression of synchronized oscillatory activity across BG nuclei in the beta (β) frequency range (12-30Hz) in humans or experimental parkinsonism [16,17]. These synchronized oscillations were first associated with tremors [7] but seem to be better correlated with akinesia/rigidity [13,18,19]. Unlike spike-rate changes, their generation mechanisms remain unknown. From a theoretical perspective, any neuronal networks incorporating negative feedback loops with delays can generate oscillatory activity patterns [20]. The multiple parallel and recurrent inhibitory feedback loops in the BG network include many circuits that, in theory, could generate PD-related β-synchronization [21–23]. The first BG pattern generator system identified was the reciprocally connected subthalamic nucleus (STN) and globus pallidus (GP) circuit [24,25]. The organization of GP into prototypic and arkypallidal neurons might also constitute a key neuronal substrate to propagate these β-oscillations in BG loop [26,27]. However, alternative circuit generators have also been proposed in the cortex [28], the striatum [29], and other BG networks [21,30,31]. In particular, the cortex is a strong rhythm generator [32,33] that presents abnormal β-synchronization during PD [34]. As such, one attractive hypothesis is that the parkinsonian β-oscillations might be generated in the cortex and abnormally maintained/amplified by GP-STN network [28,35] or the hyperdirect pathway [23,30]. However, the specific contribution of these different circuit components has never been tested with population-specific and millisecond time-scale control of neuronal networks. In this study, we combined *in vivo* electrophysiological recordings in normal and parkinsonian rats with optogenetic manipulations (i.e. opto-excitation and opto-inhibition) to dissect the specific functional contribution of key cortico-basal ganglia (CBG) components (i.e. the motor cortex, the STN, and the GP) and understand how the generation/propagation of abnormal firing rate and synchronized oscillatory activity in PD is orchestrated.

RESULTS

mCx activity is not necessary for abnormal β-synchronization or STN hyperactivity in 6-OHDA rats.

To test the contribution of motor cortex (mCx) in generating abnormal BG network dynamics (including both rate and synchronization changes), we micro-injected an AAV5-CaMKIIα(calcium/calmodulin-dependent protein kinase IIα)-ArchT3-EYFP virus into both primary and secondary mCx areas of 6-OHDA hemi-lesioned rats (**Figure 1A**). Opto-

inhibition of cortical neurons was confirmed using custom-made opto-electrodes (see methods) and extracellular unit recordings (**Figure 1B**). Cortical neurons were all classified as putative pyramidal cells based on action potential duration (**Figure 1C**). Most cortical neurons responded to light stimulation with a significant reduction of firing (**Figure 1D**). Quantitative analysis of the light-induced inhibition both at the individual (**Figure 1E, Table S1**) and population level (**Figure 1F**) show that the net effect was an overall strong reduction of mCx neuronal firing rate. We next characterized the impact of mCx opto-inhibition on STN firing and the level of β-synchronization in CBG circuits (**Figure 1G**). These experiments were conducted in an activated cortical state that favors the concomitant expression of both β-oscillations and STN firing hyperactivity [26,36]. We first showed that most STN neurons decrease their activity during mCx opto-inactivation (**Figure 1H**) but the inhibitory effect was moderate (**Figures 1I, J, Table S1**). Interestingly, STN average firing during mCx opto-inhibition in 6-OHDA rats was still faster than the one recorded in control (i.e. dopamine-intact) animals (**Figure 1I, Table S1**), suggesting that STN firing hyperactivity is not primarily driven by cortical inputs. We then investigated how β-oscillations' expression was affected by mCx opto-inhibition. Looking first at β-oscillations' expression in mCx electrocorticogram (ECoG) power spectrums, we found no effect of mCx opto-inhibition (**Figure 1K**). The first spectral analysis were limited to the best β-oscillations recording epochs (as determined by power, see methods) obtained in each rat. Calculation of the 12-30 Hz β-band areas under the curve (AUC) (**Figure 1L, Table S1**) and measure of the β burst dynamics (**Figures S1A-C)** reveal no significant effect of mCx opto-inhibition. The power of β-oscillations fluctuates *in vivo* between high and low β epoch. To reveal if mCx opto-inhibition had an effect on these dynamical properties of β-oscillations, we quantified the laser effect on each light stimulation by comparing the β-AUC powers ON *vs.* OFF (**Figure 1M**). To control for the dynamical nature of β-oscillations we also compared the difference between the 2 s β-AUC epoch directly preceding the OFF epochs (i.e. the 'Pre' epoch) and the β-AUC power of the OFF epoch. Interestingly, even when observing individual β epochs of various power, we did not see any significant effect of mCx inhibition on the β-$AUC_{(OFF\text{-}ON)}$ and β-$AUC_{(Pre\text{-}OFF)}$ distribution function (**Figure 1N, Table S1**). Finally, we then investigated if mCx opto-inhibition affected the spike-timing properties of STN neurons during β-oscillations and found that the mean β-phase locking of STN neurons (**Figures 1O and S1D, Table S1**) and the vector lengths (**Figure S1E**) were not significantly impaired by mCx silencing. Although, the β-band coherence between STN unit and mCx ECoG was slightly decreased during mCx inhibition (**Figures S1F, G**), this decrease could be

explained by the sensitivity of the spike-field coherence measures to firing rate level [37], as verified by randomly removing action potential in STN spike trains of the same OFF epoch dataset (**Figures S1H-J**). The contribution of other cortical areas (e.g. somato-sensory cortex) in *β*-oscillations' generation was also excluded by performing large-scale cortical ablation in 6-OHDA rats (**Figures S2A, B**). Altogether, these results rule out the contribution of mCx as a major source for the generation and the transmission of *β*-oscillations in the 6-OHDA rat model of PD.

STN activity is not necessary for abnormal *β*-oscillations expression in 6-OHDA rats.

STN neurons are highly synchronized at *β* frequencies and this activity could be important for orchestrating abnormal *β* rhythm [26,27,38]. We tested the STN contribution to *β*-oscillations' generation using an opto-inhibitory approach (**Figure 2A**) based on two different viral constructs: either an AAV5-CaMKIIα-eArchT3-EYFP virus as performed in a seminal study [39], or an AAV5-hSyn-eArch3-EYFP that contain a ubiquitous and neuron-specific promotor: the human synapsin 1 (hSyn). Qualitative (**Figure 2B, C**) and quantitative (Figures S3A, B) histological control of EYFP expression confirms the transduction of STN neurons and appropriate axonal labelling in STN target regions for both viral approaches. The efficacy of STN opto-inhibition was verified for each animal using opto-electrode mapping and the animals that did not reach satisfactory level of STN inhibition (i.e. >60%) were excluded from further analysis (see methods). For both sets of experiments, STN neuronal firing rate was strongly reduced by light stimulation (**Figures 2D, E, Table S2**). We next tested the impact of STN opto-inhibition on the expression of *β*-oscillations (best *β*-power recordings for each rat). We found that the *β* power (**Figure 2F, Table S2**) and the *β* burst duration (Figures S3C) were not affected by STN opto-inhibition whereas the *β* burst count was slightly decreased (Figure S3D).To analyze if STN opto-inhibition had an effect on *β* dynamics, we next compared all the individual *β* epochs in control *vs.* laser conditions and found either no laser effect in CaMKIIα-eArchT3-STN (**Figure 2H, Table S2**) or a small reduction in the hSyn-eArchT3-STN group (**Figure 2H, Table S2**). We also performed GP LFPs recordings in hSyn-eArchT3-STN rats to identify if *β*-synchronization was affected in BG circuits. We found that although the coherence between GP LFPs and mCx ECoG was significantly reduced (**Figure 2I, Table S2**) it was nevertheless not suppressed by STN opto-inhibition. The lack of strong effects on *β* dynamics consequent to STN opto-inhibition was further confirmed by the results of STN ablation. Indeed, we found that electrolytic lesion of the STN

did not affect the level of *β*-oscillations expression in lesioned rats (**Figures S4A, B**). In conclusion, our data reveal that, against the current assumption, STN activity in 6-OHDA rats is not involved in the generation of abnormal *β* oscillations and, at best, only play a supportive role.

Opto-patterning of STN neurons at *β* frequency does not replicate the functional properties of abnormal *β*-oscillations in normal rats.

The inability to fully suppress the activity of all STN neurons during our opto-inhibition protocol could, in theory, explain the absence of visible effect on *β*-oscillation expression. To further test if STN neurons are important for *β* generation, we artificially introduced *β*-oscillations directly at the level of STN in normal animals and dissected the functional properties and neuronal substrates of these synthetic *β*-oscillations in comparison to the parkinsonian *β* recorded in 6-OHDA rats. Reverse engineering of *β*-oscillations was achieved by directly patterning the activity of STN neurons at *β* frequency (20 Hz) using an optical excitatory (AAV-CaMKIIα-ChR2(H134R)-EYFP, **Figures 3A, B**) or an inhibitory approach (AAV-CaMKIIα-eArchT3.0-EYFP, **Figures S5A, B**). These excitatory/ChR2 and inhibitory/ArchT3.0 *β*–patterning strategies were also used to dissect the functional contribution of specific excitatory vs. inhibitory inputs to STN neurons. We first validated these tools using opto-electrode mapping in STN. As expected, opto-patterning STN neurons at *β* frequency artificially synchronized STN neurons activity at 20Hz (**Figures 3E, S5F**) and this activity could propagate to generate abnormally high level of cortical *β*-oscillations (**Figures 3C, S5D, Table S3**) and cortico-STN coherence (**Figures S6A, B**). Interestingly, these STN opto-patterning protocols were more efficient at generating abnormal *β* synchronizations (as measured in the ECoG) when the brain state of the animal was activated as opposed to slow-wave oscillations. This property parallels the brain-state dependency of parkinsonian *β*-oscillations expression already described in anaesthetized [26] and awake[36] 6-OHDA lesioned rats. As such, these opto-patterning experiments were preferentially performed in an activated brain state. Combining STN-ChR2 *β*-patterning with unit activity recordings of the two main population of GP neurons (i.e. the prototypic and arkypallidal cells) also reveal that synthetic *β*-oscillations could propagates to GP neurons and cause a significant increase in the temporal coupling (measured through coherence analysis) between cortex and the two populations of GP neurons (**Figures S6A, B**). We next assessed if our

synthetic β-synchronization shared the same or as many as possible functional properties as parkinsonian β-oscillations. In particular, we focused our analysis on the known STN/GP neurons spike-timing properties during these oscillations (that is the antiphase relationship between STN/prototypic and prototypic/arkypallidal neurons, as well as the in-phase relationship between STN/arkypallidal neurons [26,27]) and the associated firing rate changes (that is the hyperactivity of STN neurons vs. the decrease firing of prototypic neurons). Importantly, these fine STN/GP spike-timing features during PD β-oscillations were confirmed in our dataset (**Figure 3D**). On the contrary, artificial ChR2-induced β-oscillations did not reproduce any of the correct STN/GP phase-locking preferences (**Figure 3E, Table S3**) while ArchT3.0-induced β-oscillations reproduced the correct phase-locking value of STN neurons but not the one of GP (Figure S5F). Importantly, both these artificial β-oscillations did not replicate the stereotypical antiphase firing relationship between STN and prototypic GP neurons (**Figures 3D, S5F, G**). Instead, we found that the phase lags between STN and prototypic neurons (~57° for ChR2, **Figures 3E** vs. ~42° for ArchT3.0, **Figures S5G**) represent a time delay of 7.9 ms and 5.8 ms, respectively, compatible with a monosynaptic excitatory drive from STN inputs to prototypic neurons [40]. Interestingly though, in both cases, we could reproduce (albeit with different phase-locking values toward the cortical β-cycle reference) the antiphase relationship between prototypic and arkypallidal neurons (**Figures 3D, E and S5G**) suggesting that this opposition of phase is likely driven by prototypic neurons collateral inhibition onto arkypallidal cells. These firing relationships between STN/GP neurons were also confirmed using longer (2 s) continuous light stimulation in the ChR2 dataset (**Figures S6C-E**). Finally, considering firing rate changes induced by the ChR2 or the ArchT β-patterning, we found that, in both cases, artificial β-oscillations could not faithfully reproduce the rate changes associated with parkinsonian β-oscillations (i.e. STN hyperactivity and prototypic neurons hypoactivity [26,27]). Indeed, here ChR2 opto-patterning of STN neurons at β frequency reproduced STN increase firing (**Figure 3F, Table S3**) but also induced hyperactivity of prototypic cells (**Figure 3F, Table S3**), whereas ArchT3.0 reduced cell firing in both STN and GP neurons (Figure S5H). Taken altogether, these results obtain in lesioned and control animals invalidate the causal importance of STN neurons in driving abnormal BG network dynamics in PD rodents from specific excitatory or inhibitory inputs.

GP Opto-inhibition suppresses abnormal *β*-synchronization in CBG loop in 6-OHDA rats.

The dichotomous organization of the GP into prototypic and arkypallidal neurons has been proposed as a key neuronal substrate in PD to maintain and propagate abnormal *β*-synchronization to the whole BG circuit [27]. To test if GP activity was important for *β*-oscillations expression, we applied a global opto-inhibition approach using an AAV5-hSyn-eArch3-EYFP virus. Histological verification of the reporter EYFP protein confirms the transduction of GP neurons as shown by the dense axonal labelling in STN and substantia nigra pars compacta (SNc) and SNr (**Figure 4A**). We next verified the laser inhibitory effect and spread in GP using an opto-electrode made of 2 optic fibers (placed at 1, or 2 mm from the recording tip). Prototypic and arkypallidal neurons were identified through their distinctive electrophysiological signature (**Figure 4B)**[27,41]. Extracellular *in vivo* recordings showed that most putative prototypic neurons were significantly inhibited by light stimulation placed at 1 mm (**Figures 4C-E, Table S4**) or 2 mm above the recording electrode (**Figures S7A, C**). Putative arkypallidal neurons were also strongly inhibited by light stimulation both from the 1 mm (**Figures 4D, F, Table S4**) or 2 mm spaced fibers (**Figures S7B, D**). Overall, these in vivo GP recordings confirm that our opto-stimulation had a strong and global suppressive effect on both GP neuronal populations. We next assessed the functional impact of GP opto-inhibition onto STN firing activity and mCx ECoG during abnormal *β*-synchronization (**Figure 4G**). We first found that GP opto-inhibition produced a strong excitatory response in most STN neurons (**Figures 4H-J, Table S4**), highlighting the powerful tonic inhibitory control exerted by prototypic GP neurons onto STN activity. Similarly, *β* power analysis in mCx ECoG during GP opto-inhibition revealed a strong suppression of *β*-oscillations expression (**Figure 4K**). Both *β*-AUCs computed on the best *β* recordings (**Figure 4L, Table S4**) and on all individual *β* epochs (**Figures 4M, Table S4**) were significantly reduced in laser *vs.* control conditions. The *β* burst dynamics (i.e. duration and counts) were also strongly disrupted (Figures S7I, J). Furthermore, at the population level, the STN *β* phase-locking histogram was strongly suppressed by GP opto-inhibition (**Figure 4N**). At individual neuronal level, all phase-locked STN neurons had a significant decrease in their vector lengths value (**Figures S7E, F**) and their strength of entrainment (only 9 out of the 35 phase-locked neurons were still significantly entrained with a Rayleigh test value $p<0.05$). Also, STN spike-field coherence measures (using mCx ECoG as field) were significantly suppressed by GP opto-inhibition (**Figures S7G, H**). In conclusion, our

results strongly support the idea that GP activity is important and required for the generation of *β*-synchronization in 6-OHDA rats.

Change in the dynamical state of STN neurons firing rate do not cause *β*-synchronization suppression in 6-OHDA rats.

How changes in firing rate impact neuronal synchronization is unclear. It is thus possible that the strong increase in STN firing caused by GP disinhibition, impairs the entrainment capacity of STN neurons (i.e. single-cell level effect) or, alternatively, provides a profound change in the excitatory state of the whole BG circuit (i.e. network level effect) that might indirectly contribute to *β*-synchronizations disruption. To account for both these possibilities, we tested two approaches aimed to either mimic the increase of STN firing rate either at the single-cell level (i.e. juxtacellular approach) or at the network level (i.e. opto-excitation of STN). Juxtacellular stimulation of STN neurons using current injection (**Figure 5A**) was sufficient to significantly increase the firing activity of single STN neurons during *β* synchronization (**Figure 5B**). The intensity of current injection was adapted for each STN neuron to induce a sufficient excitation level (**Figure 5C, Table S5**). Quantification of STN neurons' frequency modulatory index (MI) showed that the excitatory effect induced by current injection was similar (albeit slightly higher) than the one obtained following GP opto-inhibition (**Figure 5D, Table S5**). Such depolarization, at the single cell level, did not affect the capacity of STN neurons to be phase-locked to *β*-oscillations (**Figure 5E, Table S5**). Indeed, all excited STN neurons were still entrained by *β*-oscillations during the ON-juxtacellular epochs with no effect on the mean phase angles (**Figure S8A**) and a slight diminution of the vector lengths (**Figure S8C**). Also, the *β*-band coherence between STN unit and mCx ECoG was significantly increased during juxtacellular stimulation (**Figures S8E, G**), and this effect was likely due to the increase in the firing rate (see **Figure S1I**). To test if a global change in BG network dynamical state was responsible for *β* synchronization disruption, we performed global STN opto-excitation **(Figure 5F**). Qualitative histological observation (**Figure 5G**) revealed sufficient STN transduction while our *in vivo* recordings confirmed the excitatory effect on STN neurons (**Figure 5H**). We could thus reproduce using opto-stimulation an overall level of STN excitation similar to the one obtained with GP silencing (**Figure 5I)** and the change in MI were not statistically different in both conditions (**Figure 5J, Table S5**). This strong increase in STN excitatory drive did not impair, nor boost *β*-oscillations power in mCx (**Figure 5K, Table S5**). The *β*-phase locking of STN neurons was slightly shifted to early phases (**Figure 5L, Table S5**) but most STN neurons were still

significantly entrained by β-oscillations (n=23/27, Rayleigh test $p<0.05$) with a small decrease of both mean phase angles (**Figure S8B**) and vector lengths (**Figure S8D**). The β-band coherence between STN unit and mCx ECoG was not affected by light stimulation (**Figures S8F, H**). These results support the idea that β-oscillations suppression following GP opto-inhibition was not caused by a dynamical change in STN excitatory state but rather due to the loss of GP contribution in orchestrating β-rhythm across CBG circuits.

Opto-patterning of GP neurons at β frequency generates β-oscillations with similar functional properties as rodents' parkinsonian β-oscillations.

During natural β-oscillations, the tonic firing activity of prototypic neurons is strongly decreased as compared to control animals [27,42] despite receiving more excitation from a hyperactive STN [36]. In addition, GABAergic D2-MSNs neurons, which increase their activity following DA loss [10], become selectively entrained at β frequency [43]. These data suggest that inhibitory striatal inputs rather than STN excitation might shape GP abnormal neuronal dynamics (i.e. decrease in firing rate and β-synchronization). We tested this hypothesis using an opto-inhibitory patterning strategy to artificially introduce β-oscillations at the level of GP neurons (**Figure 6A**). The injection of AAV5-hSyn-eArch3-EYFP virus was performed in the GP of normal rats and confirmed by histological verification (**Figure 6B**). Rhythmic optogenetic inhibition of GP neurons at 20Hz induced β-oscillations expression in mCx (**Figure 6C, Table S6**) and increase β frequency coherence of STN/GP neurons toward mCx (**Figures S9A, B**) which was due to strong β-phase locking of STN/GP neuronal populations (**Figure 6E**). As previously, we compared the spike-timing relationship and phase-locking values induced by this synthetic β (**Figure 6E, Table S6**) with parkinsonian β (**Figure 6D, Table S6**) for prototypic, STN and arkypallidal neurons. In contrast to the results obtain with the STN β-patterning, we found here that the phase-locking values of prototypic and STN neurons towards synthetic cortical β-oscillations were similar to the one measured in 6-OHDA rats. Importantly, we could also reproduce the antiphase relationship typically present between prototypic and STN neurons in PD condition, suggesting that STN β-synchronization is shaped as a consequence of GP prototypic activity and not the reverse. However, unlike our previous STN opto-patterning experiments, GP opto-inhibition did not reproduce the opposition of phase classically present between arkypallidal and prototypic neurons during β-rhythm. This was likely caused by the fact that our GP inhibitory effect was global and affected both the activity of arkypallidal and prototypic neurons. This finding hints towards

the possibility that the inhibitory inputs shaping the parkinsonian β-oscillations preferentially impact onto prototypic neurons (as did STN inputs) and not arkypallidal neurons. In addition, considering firing rates, these β-pattern optogenetic manipulations of GP reproduced the directional firing rate changes classically described in prototypic and STN neurons during parkinsonian β-oscillations, that is: a significant decrease in prototypic activity and a significant increase in STN activity. The inhibitory influence of GP neurons on STN firing was also evident using longer (2 s) and continuous light stimulation (**Figure S9C**). Indeed, as in 6-OHDA lesioned rats, the baseline STN firing rate level in control animals was strongly dependent upon GP activity (**Figures S9D, E**). These experiments also reveal the existence of an inverse correlation between the baseline firing rate of STN neurons (i.e. Frequency OFF) and the disinhibition amplitude induced by GP opto-inhibition (**Figure 6G**). Interestingly, this correlation was weaker in PD rats as compared to control animals (**Figure 6G, Table S6**), thus arguing that the control of STN neurons firing rate by GP neurons was partly occluded in 6-OHDA lesioned animals as evinced by the higher baseline firing of STN neurons. Altogether, these results show that the generation of abnormal β-synchronization requires a state of increase incoming inhibition to GP prototypic neurons and that prototypic neuronal activity plays a key role in controlling firing rate level and orchestrates neuronal synchronization in STN neurons in both normal and pathological conditions.

Discussion:

In this work, we used optogenetic stimulation, which provides fast, reversible, and population-selective neural manipulation to shed light on the functional contribution of mCx, STN and GP to the expression of CBG neural dynamics in control and hemi-parkinsonian rodents.

Cortical activity is not necessary to generate parkinsonian β-oscillations

One influential hypothesis suggests that β-oscillations are generated from cortical sources in normal and pathological conditions, which then propagates to BG circuits (i.e. particularly through the cortico-STN 'hyperdirect' pathway) where they become abnormally amplified in parkinsonism to reach pathophysiological levels [44]. Functional coupling analyses, applied to data recorded from PD patients [45–48] and animal models of parkinsonism [49] have shown that cortical β-oscillations precede in time STN abnormal oscillatory activity, arguing for a cortical drive. However, such phase-differences analyses might not necessarily vouch for

causal interactions. Here, we directly tested the cortical β-generation hypothesis using widespread mCx opto-inhibition in a rat model of PD (Figure S10A). We found that mCx inactivation or large-scale cortical ablation did not alter the level of abnormal β-oscillations expression in CBG circuits. Opto-inhibition of mCx also had a weak effect on STN firing rate hyperactivity which is not entirely surprising. First, STN neurons have autonomous pacemaker firing properties [50], and there is good evidence that the cortico-STN transmission is profoundly reduced in both rodent and monkey PD models [51,52]. The capacity of parkinsonian β-rhythm to synchronize BG circuits in a cortex-independent manner could therefore represent a novel pathological feature of these oscillations. Indeed, if cortical activity can no longer control spike-rate and synchronization changes in BG circuits, this could certainly impair the information processing flow, leading to functional deficits. Re-establishing cortical control over BG activity might restore some level of functionality in these circuits and could potentially explain the reduction of parkinsonian signs observed following cortical deep brain stimulation [34,39,53]. Altogether, our results argue against a cortical origin of parkinsonian β-oscillations and rule out a significant contribution of the hyperdirect pathway in driving STN hyperactivity or β-oscillatory activity [54]. Importantly though, these results do not exclude the possibility that the spontaneous and transient β-oscillations classically recorded in dopamine-intact conditions during movements are generated through cortical mechanisms [55–58]. Indeed, it remains to be addressed whether parkinsonian β-oscillations originate from dysregulation in space and time of normal β-oscillations [59,60] or whether they are generated through entirely different circuit mechanisms.

STN neurons are not necessary for parkinsonian β-oscillation synchronization

The STN firing-rate increase and synchronized β-oscillatory activity represent a stereotypical hallmark of parkinsonism [36,38,61], and these changes could contribute to a stronger functional impact of STN neurons onto CBG activity in the PD state [38]. In addition, the STN is reciprocally-connected to GP neurons [62] and this microcircuit forms a negative feedback loop that has been proposed to generate [24], amplify [25], or propagate synchronized oscillatory activity *in vivo* [26] (Figure S10B). The intrinsic properties of STN neurons could also reinforce abnormal oscillatory activity through post-inhibitory rebound activity [63,64]. However, we show here that STN opto-inhibition, opto-excitation, and lesion had very limited effect on parkinsonian β-oscillation expression. In addition, reintroducing β-oscillations directly at the level of STN in normal animals (using β-frequency opto-patterning) did not

mirror the firing rate alterations measured in GP prototypic and arkypallidal neurons in parkinsonian rats [42]. Furthermore, it did not reproduce the correct spike-timing relationships classically observed in the PD condition between STN neurons, prototypic, and arkypallidal neurons [26]. Instead, the phase relationships we obtained when opto-exciting or opto-inhibiting STN inputs are consistent with a preferential functional impact onto prototypic neurons (causing an in-phase relationship with STN), and an opposite response in arkypallidal neurons (causing an anti-phase relationship) likely driven by disynaptic inhibition. The excitatory response induced in prototypic neurons upon STN activation has a short synaptic delay (<6 ms) compatible with a direct monosynaptic STN drive [40], whereas arkypallidal inhibition is likely driven by prototypic axon collateral [27]. Such preferential integration of excitatory STN inputs onto prototypic vs. arkypallidal neurons could reflect a differential synaptic organization of STN inputs and/or a difference in collaterals inhibitory balance between the two populations of GP neurons. It is tempting to speculate that the differences of spike-timing in STN/GP network during parkinsonian β *vs.* artificial β-oscillations could be due to a reorganization of STN axonal connectivity onto GP neurons induced by the lack of dopamine which can trigger many adaptive changes affecting the functional connectivity within CBG circuits [51,65–67]. However, the anti-phase activity of GP prototypic neurons and STN neurons present after dopamine lesions is also observed in dopamine-intact animals during synchronous spike-and-wave discharges that underlie absence epileptic seizures [68]. This suggests that the temporal structure of STN/prototypic spike interactions during abnormal synchronized oscillations is imposed by GP prototypic inhibitory activity and not by STN excitatory drive. Altogether, these results cast doubt on the capacity of STN neurons to generate, propagate or amplify abnormally synchronous oscillatory activity at β-frequency in CBG circuits in a rodent model of PD.

GP activity orchestrates abnormal network dynamics in basal ganglia circuits

The functional importance of GP neurons has dramatically changed in the past two decades from being a simple relay nucleus in the indirect pathway [5,69] to being a central and integrative hub within BG circuits [70,71]. In the PD pathological state, the dichotomous organization of GP neurons has been proposed to play a key role in coordinating and broadcasting pathological network activity [26,27,72] (Figure S10C). Here, we demonstrate for the first time that GP activity is indeed necessary for the expression and propagation of abnormal β-oscillations in a rodent model of PD. We also show that GP prototypic neurons

control baseline STN firing activity both in control and PD conditions. This strong and tonic inhibitory influence likely extends to other nuclei both within and outside BG, especially considering the diverse and widespread projections of GP neurons [27,73,74]. Interestingly though, the disinhibitory effect induced in STN by GP opto-inhibition was smaller in PD as compared to control animals. These differences could be due to the decrease in prototypic neuronal firing in the PD state that contributes to STN hyperactivity and may thus partially occludes the disinhibition induced by GP opto-inhibition. As such, the synaptic adaptation that has been described for prototypic neurons (i.e. increase strength and number of synapses in STN)[66,75] might thus be a compensatory phenomenon to maintain effective inhibition onto STN neurons. The origin of the prototypic firing rate decrease observed during β-oscillations is an important question. Given the hyperactivity of STN induced by DA-loss and that it preferentially excites prototypic neurons, the most likely cause of prototypic firing reduction is the concurrent increase in inhibition coming from striatal indirect projection neurons [10,11,43]. Striatal indirect neurons become selectively entrained during β-oscillations [43] with a phase preference that precede STN activity by 45° (which corresponds to ~ 6 ms assuming a 50 ms β-cycle period)[26] so striatal β-inhibition and STN β-excitation will hit the GP at around the same time. The total number of striatal neurons far exceed those in STN [76] and this is also true for the number of synaptic contacts established in the GP [77,78]. Considering these figures, the synaptic ratio of striatal vs. STN inputs is ranging from 30:1 to 50:1, supporting the idea that GP activity might be primarily controlled by striatal inhibition during excessive neuronal synchronization. We confirm here that rhythmic inhibition of GP neurons reproduces the correct spike-timing and firing rate relationship classically measured during parkinsonian β-oscillations between STN and prototypic neurons. The importance of increased striatal inhibition to induce abnormal oscillatory activity in GP has been suggested by many computational studies [79,80] but how this increase leads to the generation of synchronization at β-frequency is not currently clear. One possibility is that increased striatal inputs trigger a switch of GABAergic control within GP from a state dominated by local collateral inhibition that favor GP decorrelated firing mode [81,82] to a state driven by striatal inputs that favor GP neuronal correlations. The contribution of arkypallidal neurons, which send dense inhibitory projections onto striatal neurons [27,41], or the projections from a subpopulation of prototypic neurons that selectively contact striatal GABAergic interneurons [83] could further promote the amplification of β-synchronization [31].

Conclusion on the circuit mechanisms generating β-oscillations

Whether β-oscillations are an emerging property of the striatum [29], the striatal-GP microcircuit, or a larger feedback loop that includes the thalamus [84] is not known but will be important to address in future experiments. Another important aspect would be to determine if similar circuit mechanisms apply to the generation of abnormal β-synchronization in PD primates. Indeed, correlation analyses have shown that β-synchronization in primate GP seems to be principally driven by STN and not striatal activity [38]. In addition, the STN appears to be necessary for the expression of β-oscillations in MPTP-treated monkeys [35,85]. The contribution of the striatum is less clear: blockage of GABA transmission in the GP does not affect/suppress β-oscillatory activity [35,85] and, despite the reduction of GP activity in MPTP primate as compared to control animals [38], there is still some debate as to whether striatal activity is increased [86,87] or not [38]. Altogether, our data draws strong and testable predictions that might help in resolving these issues. Indeed, if STN activity drives β-synchronization in primates, then STN activity should have an 'in-phase' relationship with the main population of GP neurons (i.e. the prototypic). We show here however that the scenario leading to the generation of abnormal β-oscillations dynamics in PD rodents is different and principally relies on inhibitory mechanisms that are orchestrated and broadcasted to the CBG network by GP neurons.

Acknowledgements: This work was supported by grants from the French Agence Nationale de la Recherche (ANR-14-CE13-0024-01 and ANR-15-CE37-0006), from the CNRS PEPS Idex Bordeaux (UB101 CR-2014R), and the LABEX BRAIN ANR-10-LABX-43. B. de la Crompe was supported by a fellowship from French Ministry (Higher Education, Research and Innovation), from France Parkinson nonprofit organization (UB320 CR-3219R), and from the LABEX BRAIN (UB106 CR-3219R). We are grateful to Dr. Hansel, and Dr. Magill for insightful scientific discussions; Dr. Deffains, Dr. Baufreton, and A. McDonald for comments on the manuscript. The authors declare no competing financial interests.

Author Contributions: Conceptualization, B.C., T.B., and N.M.; Methodology, B.C., A.A., and N.M.; Formal Analysis and Software, B.C., A.L., and N. M.; Investigation, B.C., A.A., S.A. and N.M.; Writing – Original Draft, B.C.; Writing – Review and Editing, N.M.; Funding Acquisition, N.M.; Resources and Supervision, N.M.

Declaration of Interests: The authors declare no competing interests.

Figure 1

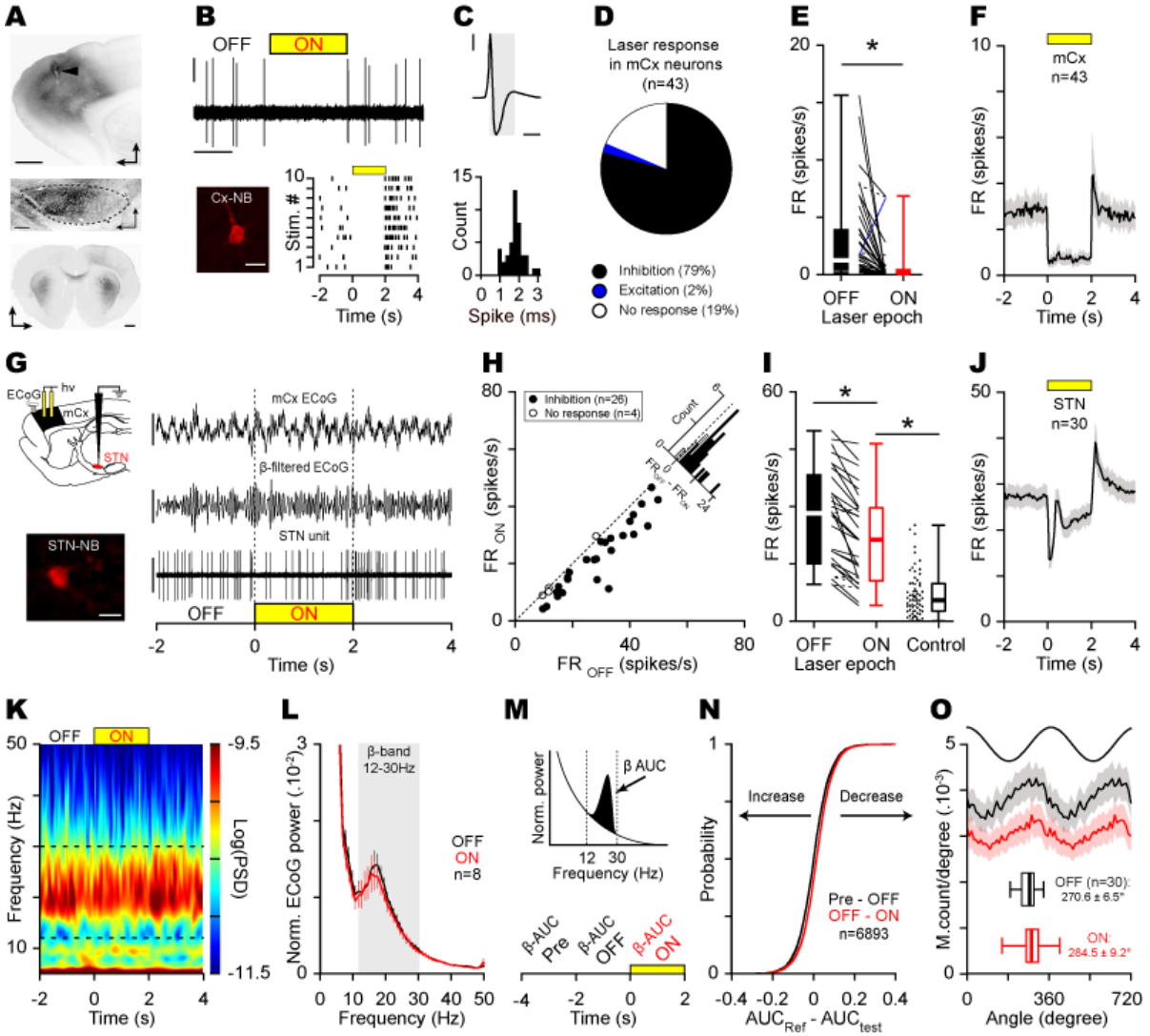

Figure 1. Motor cortex activity is not necessary for abnormal network dynamics in cortico-BG loop. (A) Epifluorescent images showing eArchT3-EYFP labelling in mCx (top, scale: 1 mm), STN (middle, scale: 200 µm), and striatum (bottom, scale: 1 mm) of 6-OHDA rats. Arrowhead indicates the optic fiber track in mCx. **(B)** Opto-inhibition example of a pyramidal neuron (top, scales: 0.5 mV, 1 s) labelled juxtacellularly with neurobiotin (bottom left, scale bar: 20 µm) and corresponding raster plot (bottom right). **(C)** Example of action potentials waveform average (top, scales: 0.5mV, 1 ms, same neuron as in B) and spike duration distribution for mCx recorded neurons (bottom, bin: 0.2 ms). **(D)** Proportion of mCx neurons inhibited (black), excited (blue), or not-modulated (white) by laser stimulation. **(E)** Box-and-whisker plots comparing mCx firing rate during OFF/ON laser epochs; firing rate (FR). **(F)** Population PSTH in mCx during laser stimulation (bin: 50 ms). **(G)** Experimental paradigm (top left) and representative example of ECoG (top right, scales: 100 µV), *β*-filtered ECoG signal (12-30 Hz, middle right, scale: 50 µV), and one STN unit (bottom right, scale: 2 mV) during mCx opto-inhibition. Juxtacellular neurobiotin labelling confirmed STN recordings (bottom left, scale: 20 µm). **(H)** Scatter plots of STN neurons firing rate during ON *vs.* OFF laser stimulation. **(I)** Box-and-whisker plots of STN firing during OFF/ON laser epochs in PD rats, and in control animals. **(J)** Population PSTH of STN firing during mCx opto-inhibition (bin: 50 ms). **(K)** Peri-event spectrogram of mCx ECoG recording during mCx opto-inhibition. **(L)** Mean normalized power spectrum of mCx ECoG during OFF *vs.* ON laser epochs (analysis on the best *β* epochs for each rat). **(M)** Schematic of the *β*-AUCs calculation (top) that we performed at three consecutive time periods: 'Pre', 'OFF', and 'ON' laser stimulation (bottom) for every single opto-stimulation epoch. **(N)** Cumulative distribution function of the *β*-AUCs differences calculated between $AUC_{(Pre-OFF)}$ and $AUC_{(OFF-ON)}$ for every ECoG *β* epochs. **(O)** Mean phase histograms of STN neurons during *β*-oscillation for the OFF and ON laser epochs. Group data represents mean ± SEM, box-and-Whisker plots indicate median, first, third quartile, min and max values. See also Table S1.

Figure 2

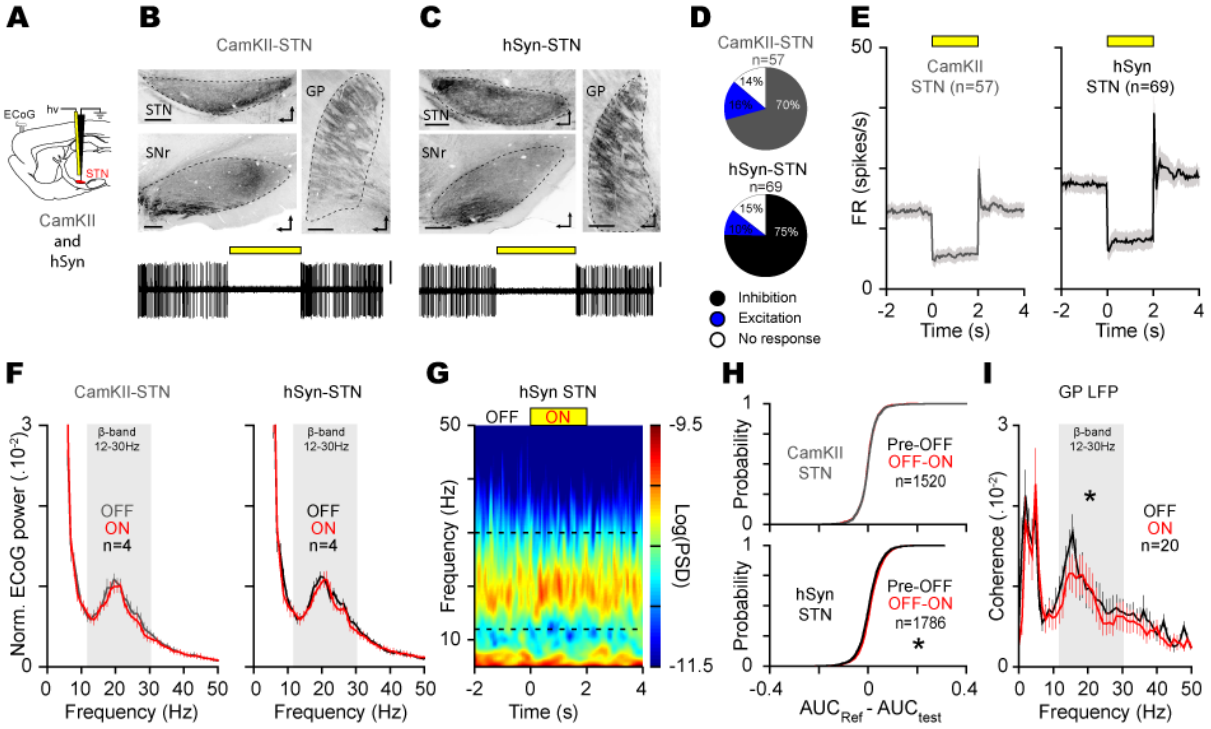

Figure 2. STN activity is not necessary for abnormal *β*-synchronization in cortico-BG loop. (A) Schematic of STN opto-inhibition using CamKII or hSyn promotor-dependent virus in 6-OHDA rats. **(B-C)** Sagittal epifluorescence images (top) showing the EYFP expression in STN and the axonal labelling in GP and substantia nigra pars reticulata (SNr). Bottom traces show examples of STN neuron opto-inhibition in CamKII-STN **(B)** or hSyn-STN **(C)** conditions (slice orientation: dorso-rostral, scale: 400 µm, scales: 0.5 mV, 6 s recording). **(D)** Proportion of STN neurons inhibited (black), excited (blue), or non-modulated (white) by the laser stimulation in CamKII-STN and hSyn-STN. **(E)** Population PSTH of STN firing during opto-inhibition in CamKII-STN (bin: 50 ms) and hSyn-STN groups (bin: 50 ms). **(F)** Mean normalized power spectrum of mCx ECoG (analysis on the best *β* epochs recordings) during OFF and ON laser stimulations in CamKII-STN (left) and hSyn-STN (right). **(G)** Example of peri-event spectrogram of mCx ECoG recording during STN opto-inhibition in hSyn-STN rat. **(H)** Cumulative distribution function of the *β*-AUCs differences calculated for $AUC_{(Pre–OFF)}$ *vs.* $AUC_{(OFF–ON)}$ for all ECoG *β* epochs in CamKII-STN (top) and hSyn-STN (bottom) conditions. **(I)** Mean coherence for ECoG *vs.* GP LFP at *β* frequency during OFF and ON laser stimulation in hSyn-STN rats. Group data are mean ± SEM. See also Table S2.

Figure 3

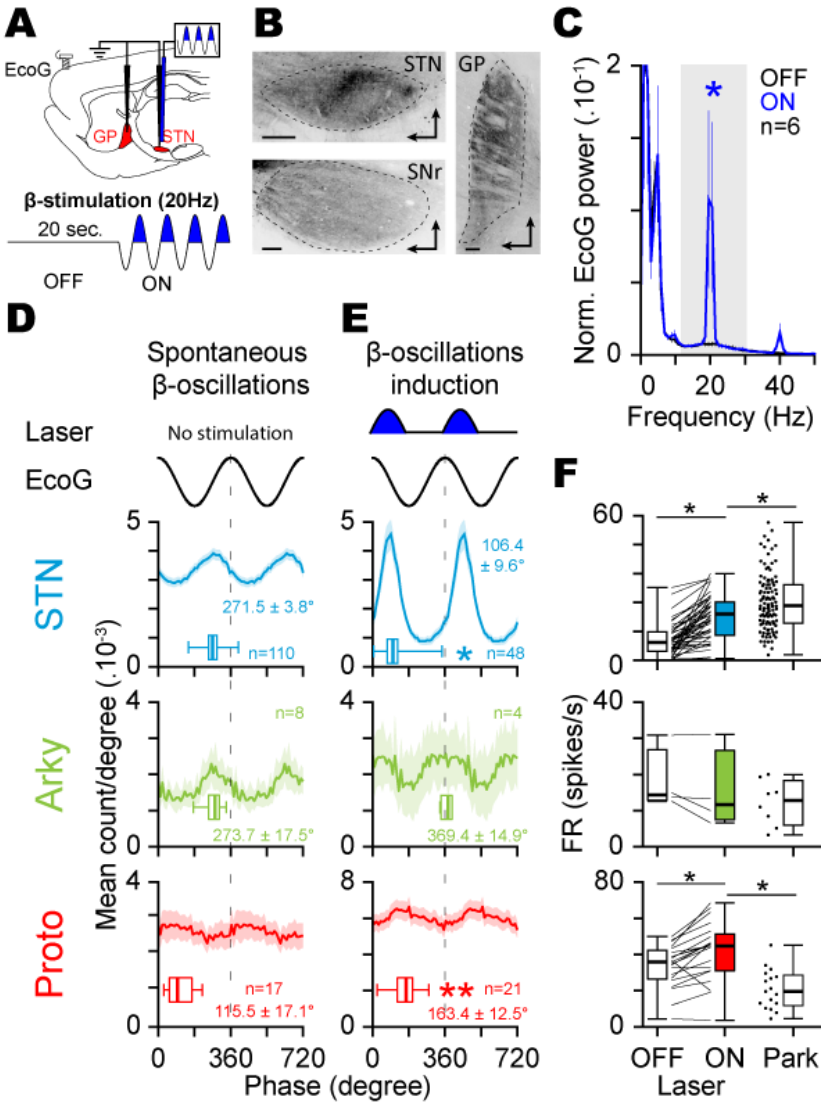

Figure 3. Excitatory optogenetic patterning of STN neurons at *β* frequency does not replicate the functional properties of parkinsonian *β*-oscillations. (A) Schematic of the experiment in ChR2-expressing STN neurons (top) and laser stimulation protocol (bottom) used to mimic abnormal *β*-oscillations in normal rats. **(B)** Sagittal epifluorescence images showing the ChR2-EYFP labelling at the level of the STN (top left) and their axons in SNr (bottom left) and GP (right) (scale: 200µm). Slices orientation: dorso-rostral. **(C)** Mean power spectrum of mCx ECoG during OFF and ON laser stimulation in normal rat. **(D)** Mean phase histograms of STN (top), arkypallidal (middle), and prototypic (bottom) neurons during abnormal *β*-oscillations recorded in 6-OHDA-lesioned rats. **(E)** Mean phase histograms of STN (top), arkypallidal (middle), and prototypic (bottom) neurons during synthetic *β*-oscillations evoked via opto-patterning of STN neurons using ChR2 in control rats. **(F)** Comparison of the change in firing rate induced by synthetic *β* as compared to abnormal parkinsonian *β* in STN, arkypallidal, and prototypic neurons. Group data represents mean ± SEM, box-and-Whisker plots indicate median, first and third quartile, min and max values. See also Table S3.

Figure 4

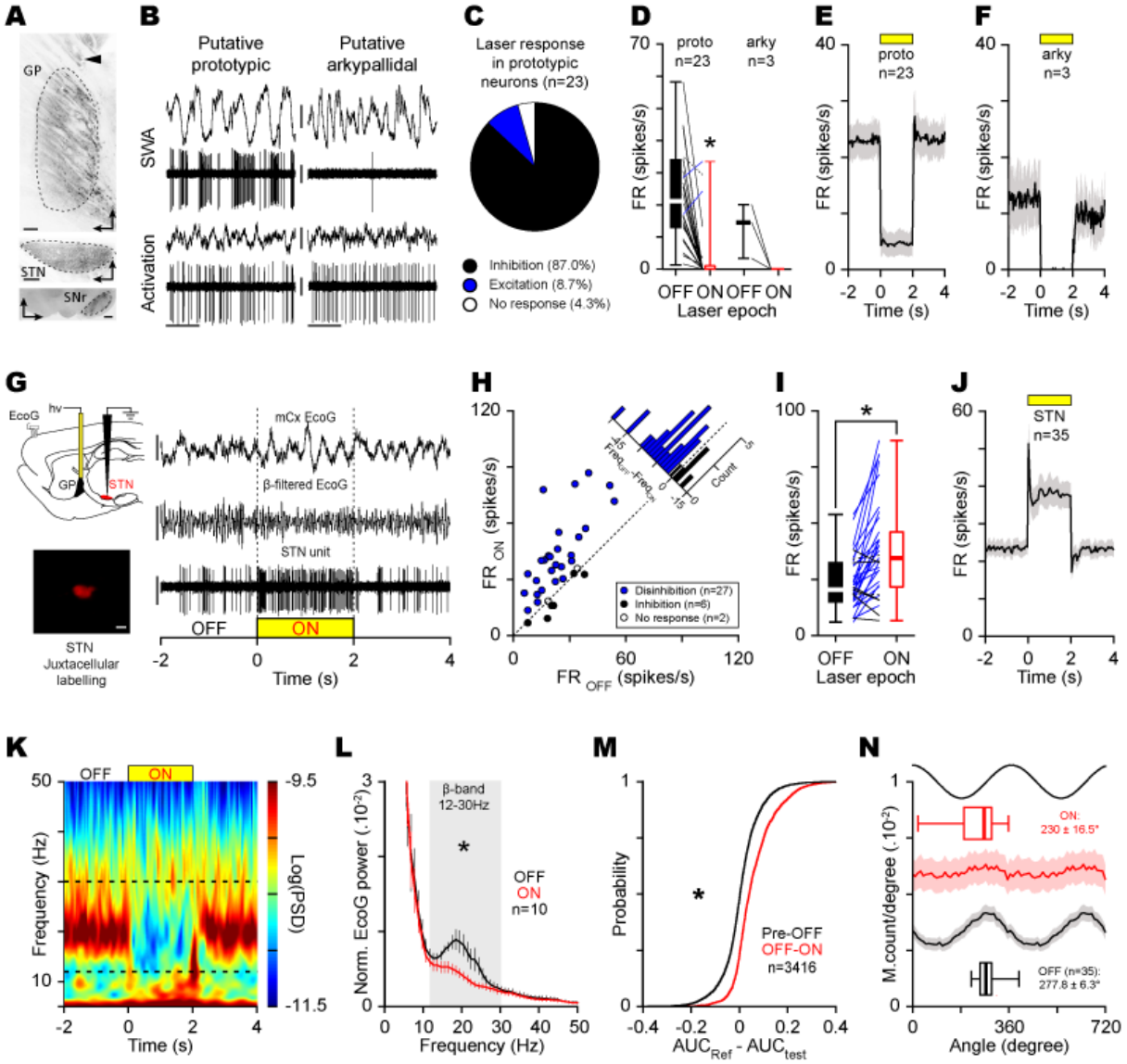

Figure 4. Globus pallidus opto-inhibition suppresses parkinsonian abnormal *β*-synchronization in cortico-BG loop. (A) Epifluorescence images showing the eArch3-EYFP labelling in GP of 6-OHDA rats (top, scale: 200 µm, arrowhead indicates the optic fiber track) and axonal labelling in STN (middle, scale: 200 µm) and SNr (bottom, scale: 500 µm). **(B)** Electrophysiological activity of prototypic and arkypallidal neurons during SWA (top) and global activation (bottom). ECoG scale: 0.2 mV; Spike unit: 0.5 mV. **(C)** Proportion of GP neurons inhibited (black), excited (blue), or not-modulated (white) by laser stimulation. **(D)** Effect of opto-inhibition on prototypic and arkypallidal firing. **(E, F)** Population PSTH of opto-inhibition on prototypic **(E)** and arkypallidal neurons **(F)**(bin: 50 ms). **(G)** Experimental paradigm (top left) and representative recordings of ECoG (scales: 250 µV), *β*-filtered ECoG (12-30 Hz, scale: 250 µV) and one STN unit (scale: 1 mV) during GP opto-inhibition. Example of juxtacellularly labelled STN neuron (bottom left, scale: 20 µm). **(H)** Scatter plot of GP opto-inhibition on STN firing. **(I)** STN firing rate changes during OFF *vs.* ON GP opto-inhibition. **(J)** Mean PSTH of STN during laser stimulations (bin: 50 ms). **(K)** Peri-event spectrogram of mCx ECoG illustrating the impact of GP opto-inhibition during *β*-oscillations. **(L)** Mean normalized power spectrum of mCx ECoG OFF *vs.* ON GP opto-inhibition (analysis on the best *β* epochs). **(M)** Cumulative distribution function of the *β*-AUCs differences calculated for $AUC_{(Pre–OFF)}$ *vs.* $AUC_{(OFF–ON)}$ for all ECoG *β* epochs during GP opto-inhibition. **(N)** Mean phase histograms of STN neurons during *β*-oscillations OFF *vs.* ON laser epochs. Group data represents mean ± SEM, box-and-Whisker plots indicate median, first and third quartile, min and max values. See also Table S4.

Figure 5

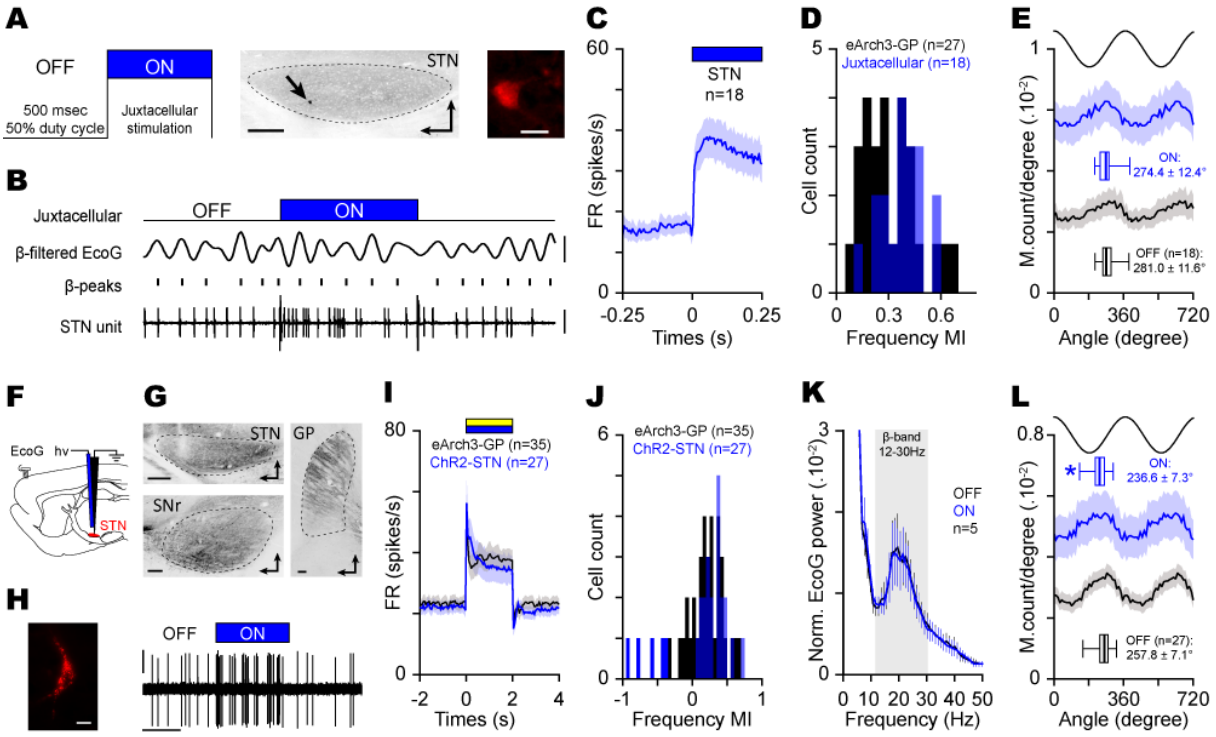

Figure 5. Change in STN firing rate does not suppress abnormal *β*-synchronization. (A) Juxtacellular stimulation protocol used to increase the firing rate of single STN neuron as revealed by neurobiotin labelling on sagittal STN epifluorescence image (left image: arrow indicate cell body labelled, scale: 200µm; right image: neurobiotin-labelled STN neuron, scale 20 µm). **(B)** Example of STN neuron firing increase during juxtacellular stimulation (scales bars are *β*-filtered ECoG: 50 µV, Spike: 2 mV, Time: 750 ms). **(C)** Population PSTH of all juxtacellularly-excited STN neurons recorded during *β*-oscillations epochs (bin: 5 ms). **(D)** Comparison of the modulatory index (MI) distribution obtained from juxtacellularly-excited STN neurons as compared to disinhibited STN neurons from eArch3-GP opto-inhibition. **(E)** Mean phase histograms of the juxtacellularly-excited STN neurons during *β*-oscillation during OFF *vs.* ON juxtacellular stimulation epochs. **(F)** Schematic illustration of the electrophysiological recordings in STN expressing ChR2-EYFP in 6-OHDA rats. **(G)** Sagittal epifluorescence images illustrating the ChR2-EYFP signal at the level of STN (top left) and axon terminals in SNr (bottom left) and GP (right). Scale bar represent 200 µm. **(H)** Example of STN opto-excitation during laser stimulation (right, scales bars are: 0.5 mV, 1 s) and labelled with neurobiotin (left, scale bar is 20 µm). **(I)** Comparison of population PSTH between all ChR2-excited STN neurons and all STN neurons during eArch3-GP opto-inhibition (bin: 50 ms). **(J)** Distribution of the MI obtained from ChR2-excited STN neurons and disinhibited STN neurons during eArch3-GP inhibition. **(K)** Mean normalized power spectrum of mCx ECoG during OFF and ON laser epochs (analysis on the best *β* epochs for each rat). **(L)** Mean phase histograms of the STN neurons during OFF and ON laser epochs. Group data represents mean ± SEM, box-and-Whisker plots indicate median, first and third quartile, min and max values. See also Table S5.

Figure 6

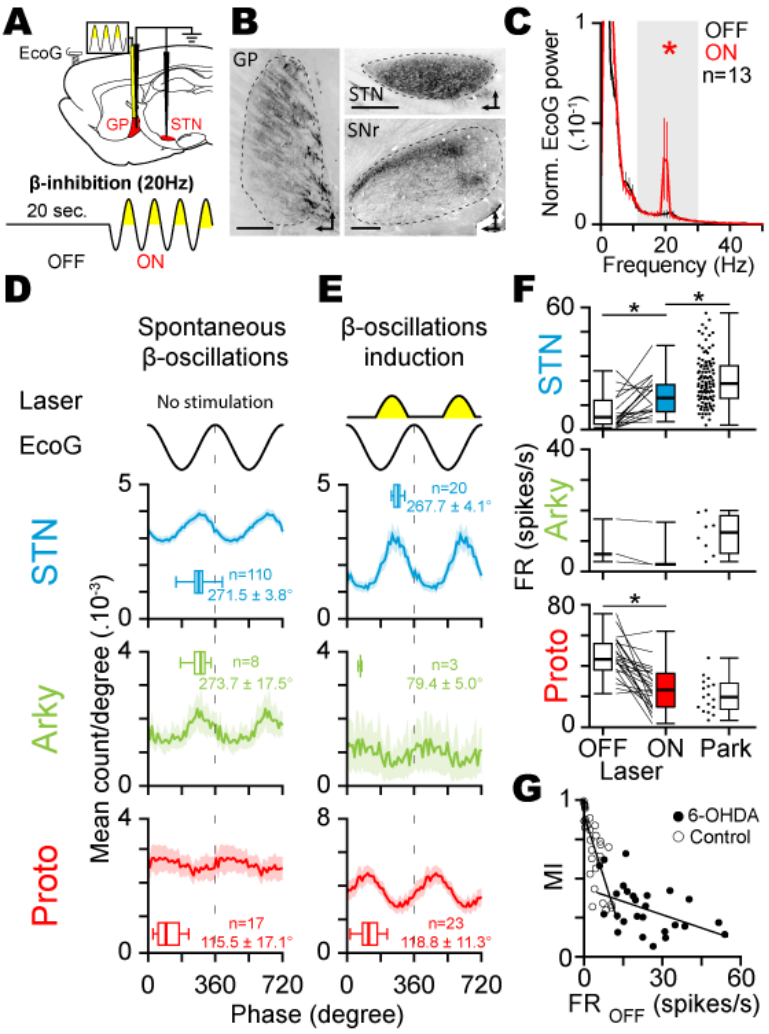

Figure 6. Optogenetic patterning of GP neurons at *β* frequency replicates the core functional properties of parkinsonian *β*-oscillations. (A) Schematic of the experiments (top) and laser stimulation protocol used (bottom) to reintroduce abnormal *β*-oscillations in control rats. **(B)** Sagittal epifluorescence image of eArch3-EYFP expression in GP (right) and target structures in STN (top left) and SNr (bottom left). Scale bars represent 400µm. **(C)** Mean normalized power spectrum of mCx ECoG during OFF and ON laser stimulations. **(D, E)** Mean phase histograms of STN (top), arkypallidal (middle), and prototypic (bottom) neurons during parkinsonian *β*-oscillations recorded in PD rats **(D)** or during synthetic *β*-oscillations generated via GP neurons opto-patterning using eArch3 in control rats **(E)**. **(F)** Comparison of the firing rate changes induced by synthetic *β* as compared to parkinsonian *β* in STN, arkypallidal, and prototypic neurons. **(G)** Scatter plots and linear regression of the MI *vs.* frequency OFF calculated for all STN neurons recorded in control animals (open circle) or parkinsonian rats (black circle). Group data represents mean ± SEM, box-and-Whisker plots indicate median, first and third quartile, min and max values. See also Table S6.

Supplemental Information:

Table S1. Relates to Figure 1

Figure	Parameter	n (rats/neurons)	Data Type	Data Value	Statistical test	significance level
1E	Firing Rate	5 /43	OFF	2.8 ± 0.6	Wilcoxon signed rank test	z=-5.23, p<0.001
			ON	0.7 ± 0.3		
1I	Firing Rate	8/30	OFF	27.3 ± 2.3	Wilcoxon signed rank test	z=-4.70, p<0.001
			ON	21.7 ± 2.2		
		15/68	Control	7.0 ± 0.7	Mann-Whitney Rank Sum Test	U=235, p<0.001
1L	β-AUC power	8/8 rec.	OFF	1.7 ± 0.1 x10^{-1}	paired t-test	t=1.69, p=0.135
			ON	1.6 ± 0.2 x10^{-1}		
1N	β-AUC power	8/6893 opto stim	Pre-OFF	1.1 ± 0.8 x10^{-3}	Wilcoxon signed rank test	z=--1.53, p=0.126
			OFF-ON	3.0 ± 0.8 x10^{-3}		
1O	β-phase locking	8/30	OFF	270.6 ± 6.5 °	Watson-Williams F test	F=1.42, p=0.240
			ON	284.5 ± 9.2 °		

Table S2. Relates to Figure 2

Figure	Parameter	n (rats/neurons)	Data Type	Data Value	Statistical test	significance level
2E, CaMKIIα	Firing Rate	4/57	OFF	16.0 ± 1.4	Wilcoxon signed rank test	z=-4.46, p<0.001
			ON	6.9 ± 1.3		
2E, hSyn	Firing Rate	4/69	OFF	21.7 ± 1.7	paired t-test	t=5.17, p<0.001
			ON	9.9 ± 1.9		
2F, CaMKIIα	β-AUC power	4/4 rec.	OFF	1.5 ± 0.3 x10^{-1}	—*	—*
			ON	1.2 ± 0.2 x10^{-1}		
2F, hSyn	β-AUC power	4/4 rec.	OFF	1.5 ± 0.03 x10^{-1}	—*	—*
			ON	1.5 ± 0.07 x10^{-1}		
2H, CaMKIIα	β-AUC power	4/1520 opto stim	Pre-OFF	1.9 ± 1.0 x10^{-3}	Wilcoxon signed rank test	z=1.11, p=0.265
			OFF-ON	-7.5 ± 1.0 x10^{-3}		
2H, hSyn	β-AUC power	4/1786 opto stim	Pre-OFF	-8.8 ± 2.6 x10^{-3}	Wilcoxon signed rank test	z=-3.63, p<0.001
			OFF-ON	4.4 ± 1.9 x10^{-3}		
2I	β-AUC coherence	4/20 rec.	OFF	1.9 ± 0.4	paired t-test	t=4.25, p<0.001
			ON	1.6 ± 0.4		

* : Sample size too small for statistical analysis.

Table S3. Relates to Figure 3

Figure	Parameter	n (rats/neurons)		Data Type	Data Value	Statistical test	significance level
3C	β-AUC power	6/6 rec.		OFF	$1.8 \pm 0.2 \times 10^{-4}$	Wilcoxon signed rank test	z=2.20, p=0.031
				ON	$4.6 \pm 0.1 \times 10^{-4}$		
3D *vs.* **3E**	β-phase locking	STN	28/110	Park	271.5 ± 3.8 °	Watson-Williams F test	F=339.15, p<0.001
			6/48	ON-ChR2	106.4 ± 9.6 °		
		Arky	6/8	Park	273.7 ± 17.5 °	—*	—*
			3/4	ON-ChR2	369.4 ± 14.9 °		
		Proto	6/17	Park	115.5 ± 17.1 °	Watson-Williams F test	F=8.97, p=0.0049
			5/21	ON-ChR2	163.4 ± 12.5 °		
3F	Firing Rate	STN	6 /48	OFF-ChR2	7.0 ± 0.8	Wilcoxon signed rank test	z=5.990, p<0.001
				ON-ChR2	15.0 ± 1.1		
			28/110	Park	24.3 ± 1.1	Mann-Whitney	U=1395 p<0.001
		Arky	3/4	OFF-ChR2	18.0 ± 4.3	—*	—*
				ON-ChR2	15.3 ± 5.4		
			6/8	Park	12.2 ± 2.2	—*	—*
		Proto	5/21	OFF-ChR2	33.7 ± 2.6	paired *t*-test	t=4.48, p=0.032
				ON-ChR2	41.7 ± 3.6		
			6/17	Park	20.8 ± 2.6	*t*-test	t=-4.52, *p<0.001*

* : Sample size too small for statistical analysis.

Table S4. Relates to Figure 4

Figure	Parameter	n (rats/neurons)		Data Type	Data Value	Statistical test	significance level
4D	Firing Rate	Proto	5/23	OFF	22.9 ± 3.0	paired *t*-test	t=5.69, $p<0.01$
				ON	4.7 ± 2.1		
		Arky	5/3	OFF	12.6 ± 4.9	—*	—*
				ON	0.03 ± 0.03		
4I	Firing Rate STN	10/35		OFF	23.8 ± 2.0	Wilcoxon signed rank test	z=4.472, $p<0.001$
				ON	38.6 ± 3.5		
4L	β-AUC power	10/10		OFF	$1.2 \pm 0.5 \times 10^{-1}$	paired *t*-test	t=4.188, $p=0.002$
				ON	$0.8 \pm 0.3 \times 10^{-1}$		
4M	β-AUC power	10/3416 opto stim		Pre-OFF	$2.7 \pm 1.1 \times 10^{-3}$	Wilcoxon signed rank test	z=-27.025, $p<0.001$
				OFF-ON	$5.6 \pm 2.3 \times 10^{-3}$		

* : Sample size too small for statistical analysis.

Table S5. Relates to Figure 5

Figure	Parameter	n (rats/neurons)	Data Type	Data Value	Statistical test	significance level
5C	Firing Rate	9/18	OFF-Juxta	23.5 ± 2.7	paired *t*-test	t=-7.62, $p<0.001$
			ON-Juxta	52.2 ± 5.6		
5D	MI	10/27	MI Arch3-GP	$3.0 \pm 0.3 \times 10^{-1}$	*t*-test	t=-1.65, $p=0.107$
		9/18	MI juxta	$3.8 \pm 0.3 \times 10^{-1}$		
5E	β-phase locking	9/18	OFF-Juxta	281.0 ± 11.6°	Watson-Williams F test	ns (F=0.29, $p=0.593$)
			ON-Juxta	274.4 ± 12.4 °		
5I	Firing Rate	5/27	OFF	22.2 ± 2.0	paired *t*-test	t=-3.96, $p<0.001$
			ON	37.3 ± 5.2		
5J	MI	10/35	MI Arch3-GP	$2.1 \pm 0.4 \times 10^{-1}$	Mann-Whitney rank sum test	ns (U=457, $p=0.831$)
		5/27	MI ChR2-STN	$1.2 \pm 0.8 \times 10^{-1}$		
5K	β-AUC power	5/5	β-AUC OFF	$2.2 \pm 0.4 \times 10^{-1}$	paired *t*-test	ns (t=0.919, $p=0.41$)
			β-AUC ON	$2.1 \pm 0.4 \times 10^{-1}$		
5L	β-phase locking	5/27	OFF	257.8 ± 7.1 °	Watson-Williams F test	F=4.90 $p=0.0313$
			ON	236.6 ± 7.3 °		

Table S6. Relates to Figure 6

Figure	Parameter	n (rats/neurons)		Data Type	Data Value	Statistical test	significance level
6C	β-AUC power	13/13 rec.		OFF	$1.2 \pm 0.2 \times 10^{-1}$	Wilcoxon signed rank test	Z=2.970, p=0.001
				ON	$1.9 \pm 0.7 \times 10^{-1}$		
6D *vs.* **6E**	β-phase locking	STN	28/110	Park	271.5 ± 3.8 °	Watson-Williams F test	ns (F=0.763, p=0.50)
			13/20	ON	267.7 ± 4.1 °		
		Arky	6/8	Park	273.7 ± 17.5 °	—*	—*
			13/3	ON	79.4 ± 5.0 °		
		Proto	6/17	Park	115.5 ± 17.1 °	Watson-Williams F test	ns (F=0.830, p=0.367)
			13/23	ON	118.8 ± 11.3 °		
6F	Firing Rate	STN	13/20	OFF	7.1 ± 1.5	paired t-test	t=-3.50, p=0.002
				ON	13.6 ± 1.8		
			28/110	Park	24.3 ± 1.1	Mann-Whitney	U=486 p<0.001
		Arky	3/3	OFF	8.8 ± 4.3	—*	—*
				ON	7.0 ± 4.6		
			6/8	Park	12.2 ± 2.2	—*	—*
		Proto	13/23	OFF	45.5 ± 2.7	paired t-test	t=5.30, p<0.001
				ON	25.9 ± 3.0		
			6/17	Park	20.8 ± 2.6	Mann-Whitney	ns (U=151, p=0.229)
6G	MI	18/32		control	y = 0.92 – 0.05x	Linear regression	p<0.001, r^2=0.60
		10/27		Park	y = 0.44 – 0.006x	Linear regression	p=0.012, r^2=0.23

* : Sample size too small for statistical analysis.

Figure S1

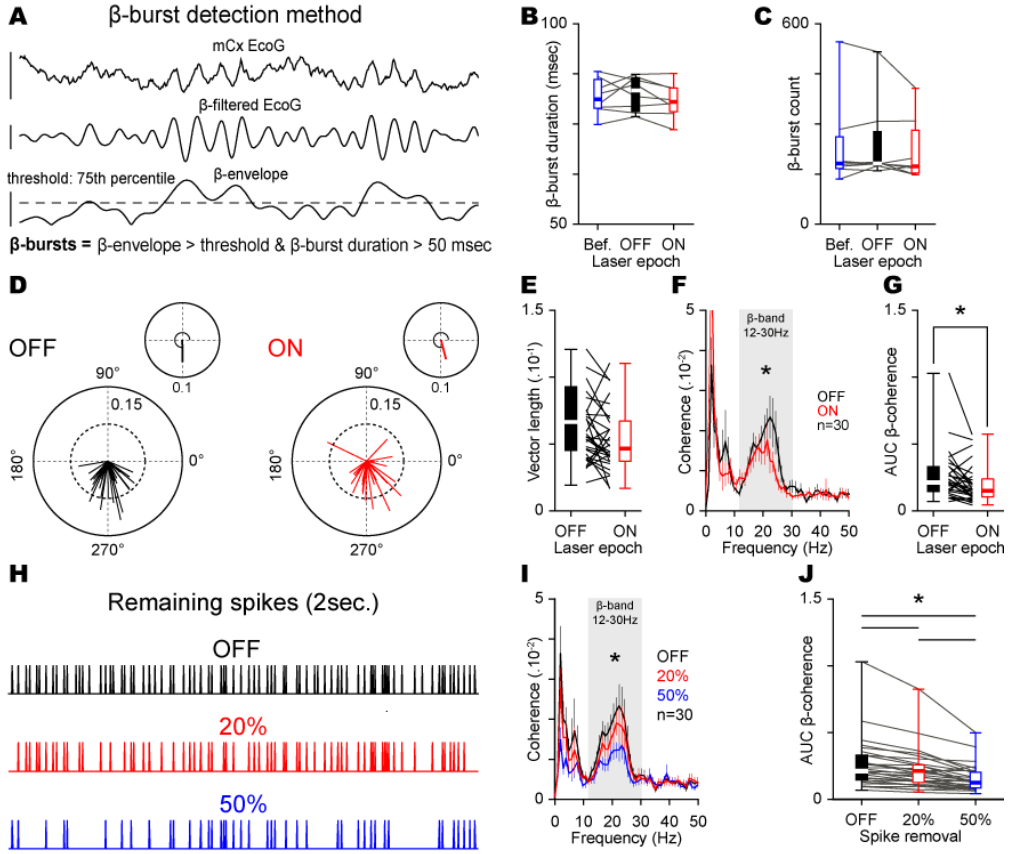

Figure S1. Effect of mCx opto-inhibition on abnormal network dynamics in Parkinsonism. (A) Analytical approach used to detect the bursts of *β* oscillations. Representative example of ECoG (scales: 200 µV), *β*-filtered signal (12-30 Hz, scale: 50 µV), and *β*-envelopes (scale: 0.04 unit) with the 75th percentile threshold (dashed line). **(B-C)** Box-and-whisker plots showing the effect of mCx opto-inhibition on the *β*-bursts duration (**B**, Before in blue *vs.* OFF in black *vs.* ON in red, n=8, *β*-bursts duration Before *vs.* OFF *vs.* ON, 8.33 ± 0.17 x10^{-2} *vs.* 8.43 ± 0.16 x10^{-2} *vs.* 8.24 ± 0.16 x10^{-2} s, One Way Repeated Measures Analysis of Variance, F=1.19, *p*=0.33) and *β*-burst counts (**C**, n=8, *β*-bursts counts Before *vs.* OFF *vs.* ON, 231.9 ± 47.37 *vs.* 235.9 ± 43.25 *vs.* 215.6 ± 32.92 *β*-bursts, Friedman Repeated Measures Analysis of Variance on Ranks, X²=0.84, *p*=0.65). **(D)** Individual and mean circular phase of phase-locked STN neurons during OFF and ON laser stimulation epochs (n=30, OFF *vs.* ON, 270.6 ± 6.5° *vs.* 284.5 ± 9.2°, Watson-Williams F test, F=1.42, *p*=0.240). **(E)** Box-and-whisker plots showing the change in vector lengths induced by mCx opto-inhibition (n=30, OFF *vs.* ON, 5.9 ± 0.4 x10^{-2} *vs.* 5.3 ± 0.4 x10^{-2}, paired *t*-test, t=1.70, *p*=0.101). **(F-G)** Mean coherence **(F)** and box-and-whisker plots of the *β*-band coherence **(G)** between mCx ECoG and STN unit during OFF and ON laser stimulation epochs (n=30, AUC *β*-band coherence OFF *vs.* ON, 2.6 ± 0.3 x10^{-1} *vs.* 2.0 ± 0.3 x10^{-1}, Wilcoxon signed rank test, z=-2.71, *p*=0.007). **(H)** Example of random spike removal reaching 20% (red), or 50% (blue) of the reference OFF stimulation epoch in one STN neuron (black). **(I-J)** Mean coherence **(I)** and box-and-whisker plots of the *β*-band coherence **(J)** between mCx ECoG and STN unit without (OFF, black) or with random spike removal (20% in red, 50% in blue, n=30, AUC *β*-band OFF *vs.* OFF 80% *vs.* OFF 50% *vs.* ON, 2.6 ± 0.3 x10^{-1} *vs.* 2.1 ± 0.3 x10^{-1} *vs.* 1.6 ± 0.2 x10^{-1} *vs.* 2.0 ± 0.3 x10^{-1}, Friedman repeated measures ANOVA on ranks, X²=50.04, *p*<0.001, following by Dunn's post hoc test, *p*<0.05 for OFF *vs.* OFF 80%, OFF *vs.* OFF 50%, OFF *vs.* ON and OFF 80% *vs.* OFF 50%, q=3.9, 6.9, 4.8 and 3.0 respectively).

Figure S2

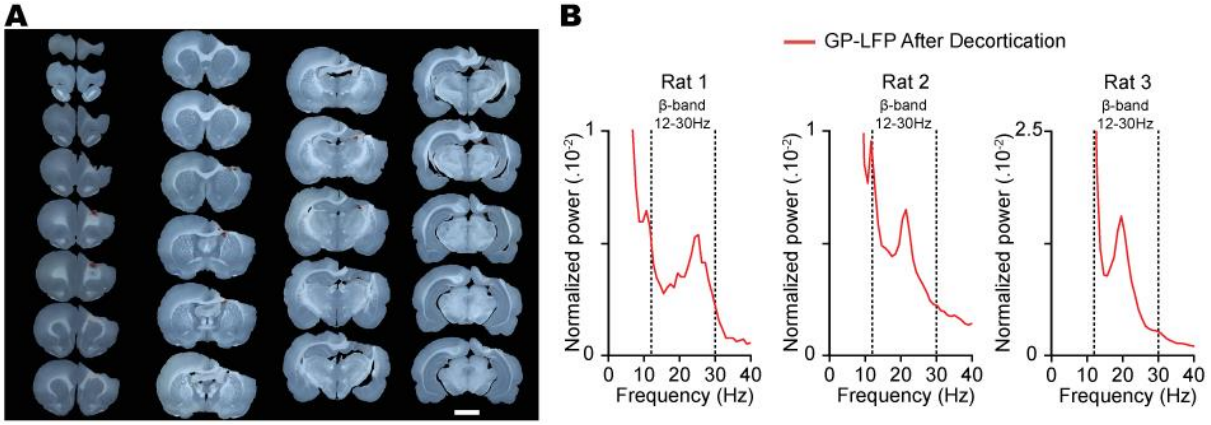

Figure S2. Decortication experiments in 6-OHDA lesioned rats. (A) Bright-field images of coronal brain sections organized in a serial manner from rostral to caudal sections and illustrating the extend of the decortication. **(B)** Power spectrums illustrating the peak in the β frequency band (12-30 Hz) present in GP local field potentials (LFPs) recorded in 3 different 6-OHDA-lesioned rats after decortication. Although the exact generation mechanism of LFPs in non-layered structure such as basal ganglia is unclear, GP-LFPs were used here as a proxy of neuronal synchronization as previously shown during β-oscillations [26].

Figure S3

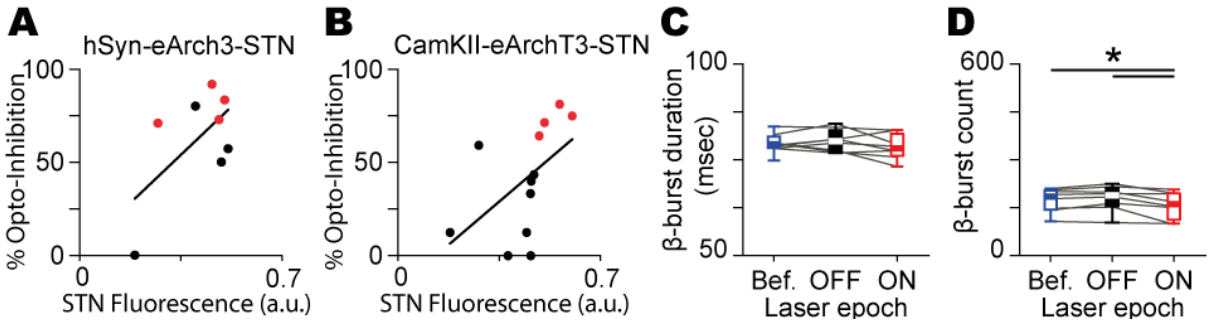

Figure S3. Quantification of STN opto-inhibition and effect on *β* bursts dynamics. (A- B) Correlation analysis between the percentage of STN opto-inhibition determined through opto-mapping experiments and the mean EYFP fluorescence in STN for hSyn-eArch3 (**A,** linear regression r^2 = 0.3741) or CamKII-eArchT3 (**B,** linear regression r^2 = 0.2664) experiments. Red and black dots indicate the animals included or excluded from the study, respectively. Animals were discarded if they had less than 10 STN neurons recorded during opto-mapping or if the total % of STN opto-inhibition was < to 60%. **(C-D)** Box-and-whisker plots showing the effect of STN opto-inhibition on the *β*-bursts duration (**C**, n=8, *β*-burst duration Before *vs.* OFF *vs.* ON, 7.96 ± 0.07 $x10^{-2}$ *vs.* 7.99 ± 0.1 $x10^{-2}$ *vs.* 7.83 ± 0.1 $x10^{-2}$ s, One Way Repeated Measures Analysis of Variance, F=1.81, *p*=0.20) and *β*-bursts counts (n=8, *β*-burst duration Before *vs.* OFF *vs.* ON, 172.75 ± 13.0 *vs.* 179.63 ± 13.9 *vs.* 157.88 ± 14.8 *β*-bursts, Friedman Repeated Measures Analysis of Variance on Ranks, F=7.19, *p*=0.007, following by Holm-Sidak post hoc test, OFF *vs.* Before, OFF *vs.* ON and Before *vs.* ON, t=1.17, 3.71 and 2.54, *p*=0.26, 0.007 and 0.047, respectively).

Figure S4

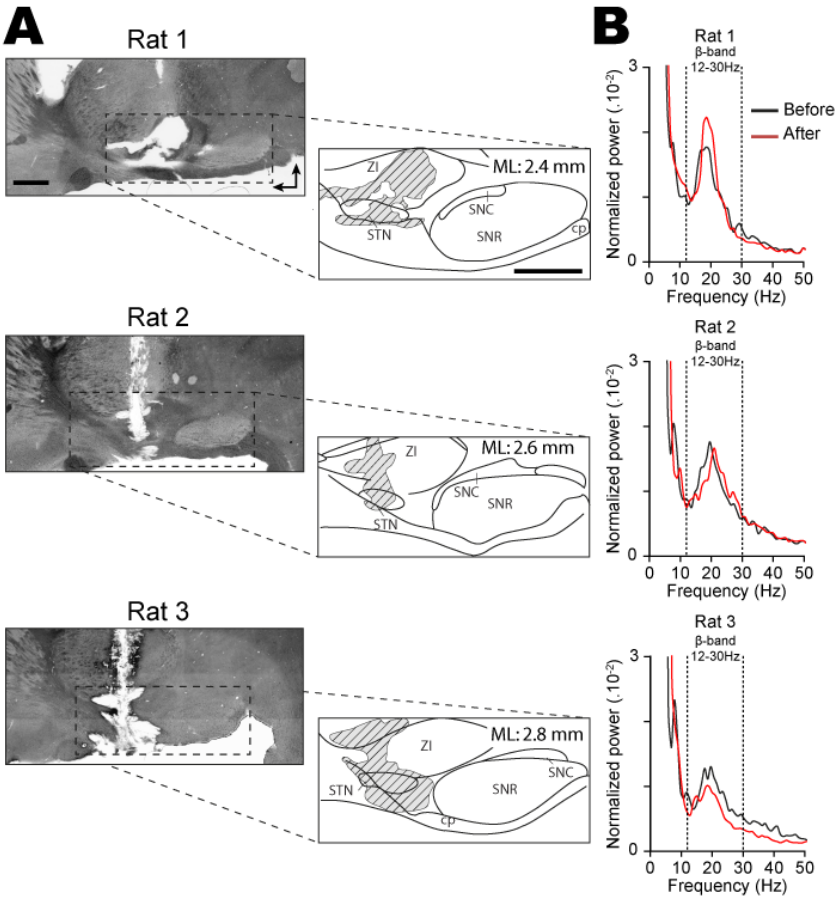

Figure S4. Effect of STN lesion on *β*-oscillations expression in 6-OHDA lesioned rats. (A) Epifluorescent images showing DAPI staining (left) and schematic representation (right) of sagittal rat brain sections illustrating the extent of the STN electrolytic lesion (hashed grey area). Scale bar represent 1 mm. **(B)** Power spectrums illustrating the peak in the *β* frequency band (12-30 Hz) present in the ECoG before and after the full lesion of the STN in 3 different 6-OHDA-lesioned rats.

Figure S5

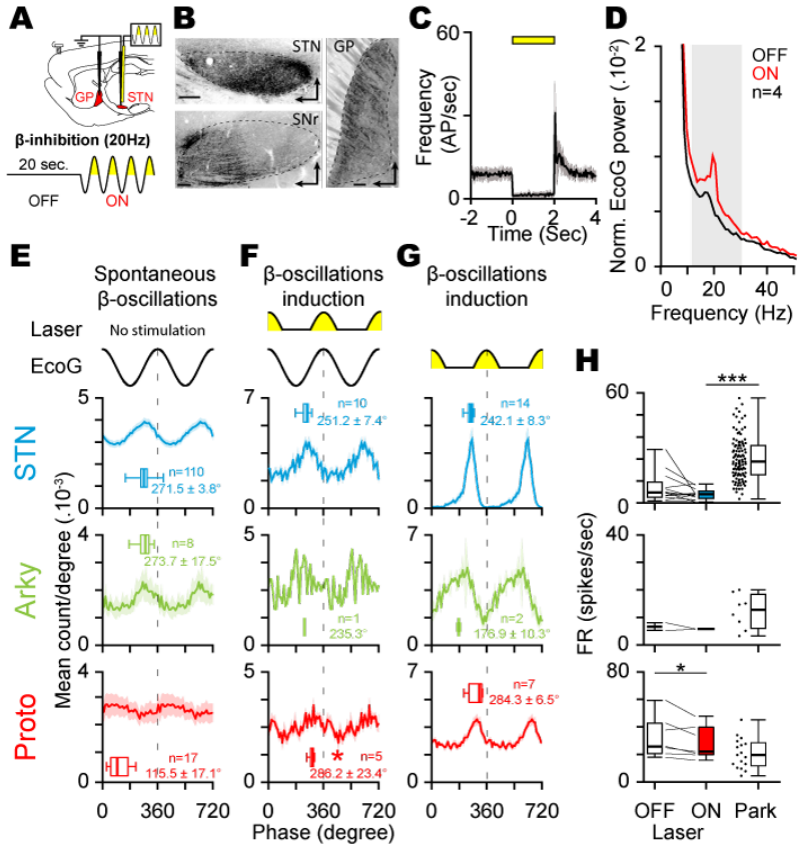

Figure S5. Inhibitory optogenetic patterning of STN neurons at *β* frequency does not replicate the functional properties of parkinsonian *β*-oscillations. (A) Schematic of the experiment in eArchT3.0-expressing STN neurons (top) and laser stimulation protocol (bottom) used to mimic abnormal *β*-oscillations in normal rats. **(B)** Sagittal epifluorescence images showing the eArchT3.0-EYFP labelling at the level of the STN (top left) and their axons in SNr (bottom left) and GP (right) (scale: 200µm). Slices orientation: dorso-rostral. **(C)** Mean PSTH of STN neurons during laser stimulations (bin: 50 ms, STN-OFF *vs.* STN-ON, n=16, 8.90 ± 2.03 *vs.* 1.37 ± 0.91 spikes/s, Wilcoxon signed rank test, z=-2.95, *p*=0.002). **(D)** Mean normalized power spectrum of mCx ECoG during OFF and ON laser stimulation in normal rat. **(E)** Mean phase histograms of STN (top), arkypallidal (middle), and prototypic (bottom) neurons during abnormal *β* oscillations recorded in 6-OHDA-lesioned rats. **(F)** Mean phase histograms of STN (top), arkypallidal (middle), and prototypic (bottom) neurons calculated from the cortical *β* oscillations signal evoked by our opto-patterned stimulation. The mean phase value of STN neurons is not statistically different in the parkinsonian *vs.* the eArchT3.0 condition (STN-Park *vs.* STN-ON, n=110 *vs.* 10, 271.5 ± 3.8 ° *vs.* 251.2 ± 7.4 °, Watson-Williams test, F=2.52, *p*=0.1153), whereas the mean phase for prototypic neurons is different (Proto-Park *vs.* Proto-ON, n=17 *vs.* 5, 115.5 ± 17.1 ° *vs.* 286.2 ± 23.4 °, Watson-Williams test, F=17.74, *p*=0.0004. **(G)** Mean phase histograms of STN (top), arkypallidal (middle), and prototypic (bottom) neurons directly calculated from the peak of the laser stimulation sine waves. These phase histograms better illustrate the phase relationships between STN and GP neurons during *β* cycles**. (H)** Comparison of the change in firing rate induced by synthetic *β* as compared to abnormal parkinsonian *β*-oscillations in STN (STN-OFF *vs.* STN-ON, n=13, 8.5 ± 2.2 *vs.* 4.9 ± 0.8 spikes/sec, Wilcoxon signed rank test, Z=-1.642, *p*=0.110; STN-Park *vs.* STN-ON, n=110 *vs.* 13, 24.3 ± 1.1 *vs.* 4.9 ± 0.8 spikes/sec, Mann-Whitney rank sum test, U=160.0, *p*<0.001), arkypallidal (Arky-OFF *vs.* Arky-ON, n=2, 6.7 ± 1.4 *vs.* 5.8 ± 0.1 spikes/sec; Arky-Park *vs.* Arky-ON, n=8 *vs.* 2, 12.2 ± 2.2 *vs.* 5.8 ± 0.1 spikes/sec), and prototypic neurons (Proto-OFF *vs.* Proto-ON, n=7, 32.8 ± 5.6 *vs.* 28.7 ± 4.5 spikes/sec, paired t-test, t=2.321, *p*=0.059; Proto-Park *vs.* Proto-ON, n=17 *vs.* 7, 20.8 ± 2.7 *vs.* 28.7 ± 4.5 spikes/sec, t-test, t=2.211, *p*=0.038). Group data represents mean ± SEM, box-and-Whisker plots indicate median, first and third quartile, min and max values.

Figure S6

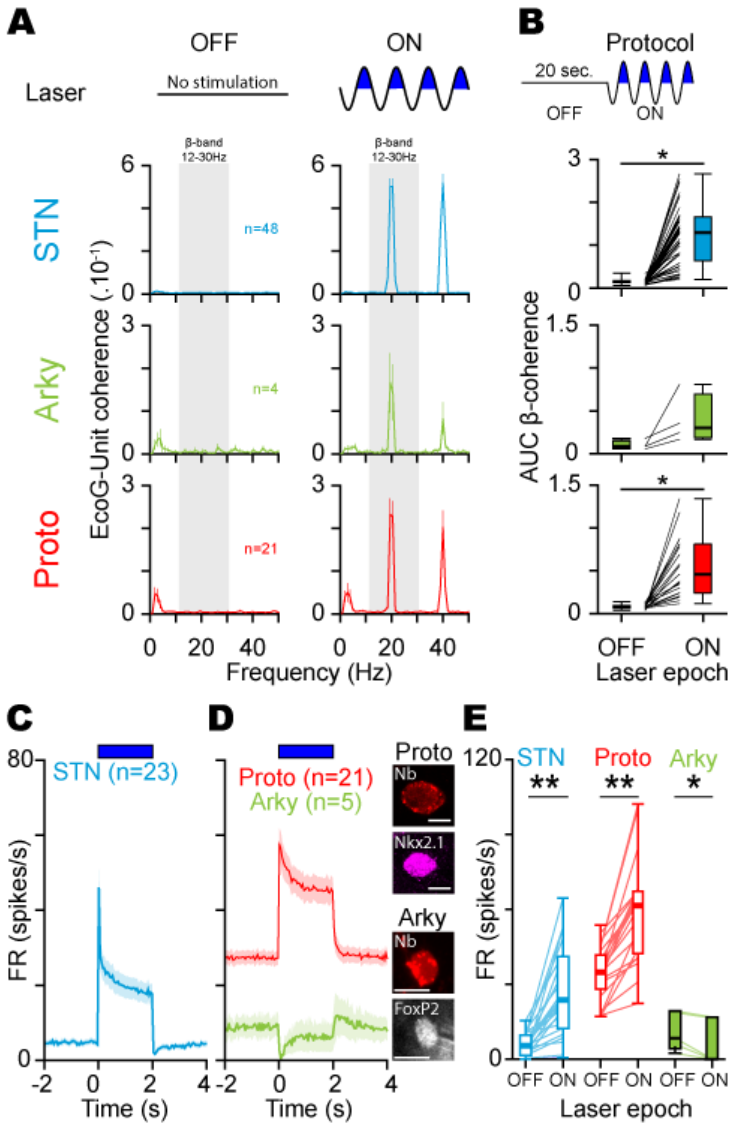

Figure S6. Optogenetic patterning of ChR2-expressing STN neurons at *β* frequency. (A) Mean Coherence calculated during the OFF *vs.* ON laser stimulation between mCx ECoG and STN (blue, n=48, AUC *β*-coherence OFF *vs.* ON: 0.1 ± 0.007 *vs.* 1.2 ± 0.09, paired *t*-test, t=-11.90, * $p<0.001$), arkypallidal (black, n=4, AUC *β*-coherence OFF *vs.* ON: 1.0 ± 0.3 *vs.* 4.0 ± 1.4 $x10^{-1}$), and prototypic neurons (red, n=21, AUC *β*-coherence OFF *vs.* ON: 0.8 ± 0.06 *vs.* 5.5 ± 0.8 $x10^{-1}$, paired *t*-test, t=-6.16). **(B)** Comparison of the *β*-coherence (12-30 Hz) OFF *vs.* ON laser stimulation (box-and-whisker plot, paired *t*-tests,* $p<0.001$). **(C)** Population PSTH of ChR2-excited STN neurons in response to a 2 s laser stimulation (n=23, firing rate OFF *vs.* ON, 5.9 ± 0.9 *vs.* 26.2 ± 3.6 spikes/s, paired *t*-test, t=-6.11, $p<0.001$). **(D)** Population PSTH of prototypic (red, n=21, firing rate OFF *vs.* ON, 34.2 ± 2.2 *vs.* 59.4 ± 4.4 spikes/s, paired *t*-test, t=-7.85, $p<0.001$) and arkypallidal neurons (black, n=5, firing rate OFF *vs.* ON, 11.0 ± 3.4 *vs.* 6.8 ± 4.1 spikes/s, paired *t*-test, t=3.44, $p=0.0260$) in response to STN opto-excitation. Confocal fluorescence images of juxtacellularly-labelled with neurobiotin (Nb; red) and identified GP prototypic Nkx2.1+ (magenta, top) and arkypallidal FoxP2+ neurons (grey, bottom). Scale bars: 10 µm. **(E)** Box-and-whisker plots comparing the firing rate during OFF *vs.* ON STN opto-excitation stimulation (paired *t*-tests, * $p=0.026$ and ** $p<0.001$).

Figure S7

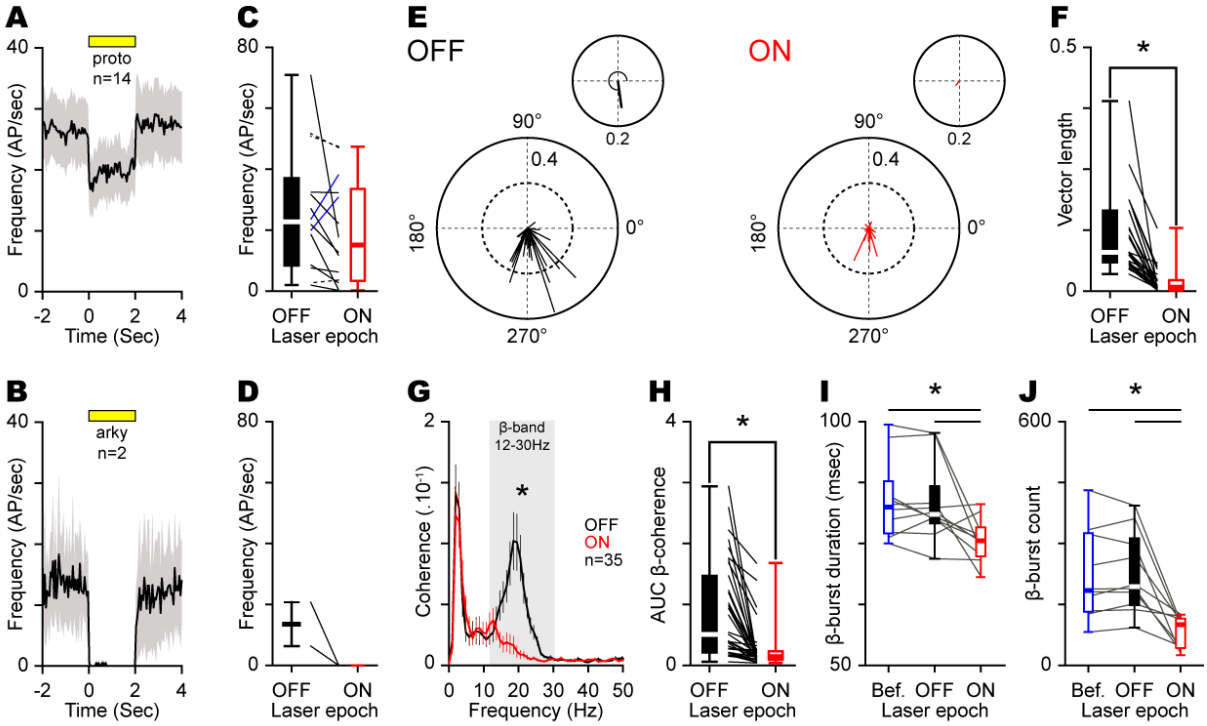

Figure S7. Effect of GP opto-inhibition on abnormal *β*-oscillations dynamics in Parkinsonism. (A-B) Population PSTH of prototypic (n=13, firing rate OFF *vs.* ON, 26.4 ± 5.4 *vs.* 19.5 ± 4.5 spikes/s, Wilcoxon signed rank test, z=-2.93, *p*=0.068) and arkypallidal neurons (n=2, firing rate OFF *vs.* ON, 13.6 ± 7.2 *vs.* 0.08 ± 0.08 spikes/s) in response to light stimulation with optic fiber placed 2 mm above the recording electrode (data represent mean ± SEM, bin: 50 ms). All these neurons were also inhibited with the laser source placed 1 mm (see figure 4). **(C-D)** Box-and-whisker plots of prototypic (Wilcoxon signed rank test, * *p*>0.05) and arkypallidal neurons during the OFF and ON laser stimulation. **(E)** Individual and mean circular phase of STN neurons entrained at *β* frequency during OFF and ON laser stimulation epochs (n=35, OFF *vs.* ON, 277.8 ± 6.3° *vs.* 230.0 ± 16.5°, Watson-Williams F test, F=0.510, p=0.478). **(F)** Box-and-whisker plots showing the change in vector lengths induced in STN neurons by GP opto-inhibition (n=35, OFF *vs.* ON, 1.2 ± 0.1 $x10^{-1}$ *vs.* 0.3 ± 0.06 $x10^{-1}$, Wilcoxon signed rank test, z=-5.16, *p*<0.001). **(G-H)** Mean coherence **(G)** and box-and-whisker plots of the *β*-band (12-30 Hz) coherence **(H)** between mCx ECoG and STN unit during OFF and ON laser stimulation epochs (n=35, AUC *β*-band coherence OFF *vs.* ON, 8.8 ± 1.3 $x10^{-1}$ *vs.* 2.7 ± 0.6 $x10^{-1}$, Wilcoxon signed rank test, z= -5,086, *p*<0,001). **(I-J)** Box-and-whisker plots showing the effect of GP opto-inhibition on the *β* bursts duration **(I,** n=10, β-burst duration Before *vs.* OFF *vs.* ON, 8.39 ± 0.26 $x10^{-2}$ *vs.* 8.31 ± 0.26 $x10^{-2}$ *vs.* 7.56 ± 0.14 $x10^{-2}$ s, One Way Repeated Measures Analysis of Variance, F=6.67, *p*=0.007, following by Holm-Sidak post hoc test, OFF *vs.* Before, OFF *vs.* ON and Before *vs.* ON, t=0.28, 3.01 and 3.30, *p*= 0.78, 0.015 and 0.012, respectively) and *β* bursts counts **(J,** n=10, *β*-burst duration Before *vs.* OFF *vs.* ON, 221.5 ± 34.78 *vs.* 226.70 ± 31.28 *vs.* 81.80 ± 12.41 *β*-bursts, Friedman Repeated Measures Analysis of Variance on Ranks, X^2=15.80, *p*<0.001, following by Dunn's post hoc test, OFF *vs.* Before, OFF *vs.* ON and Before *vs.* ON, q=0.89, 3.80 and 2.91, *p*>0.05, *p*<0.05 and *p*<0.05 respectively).

Figure S8

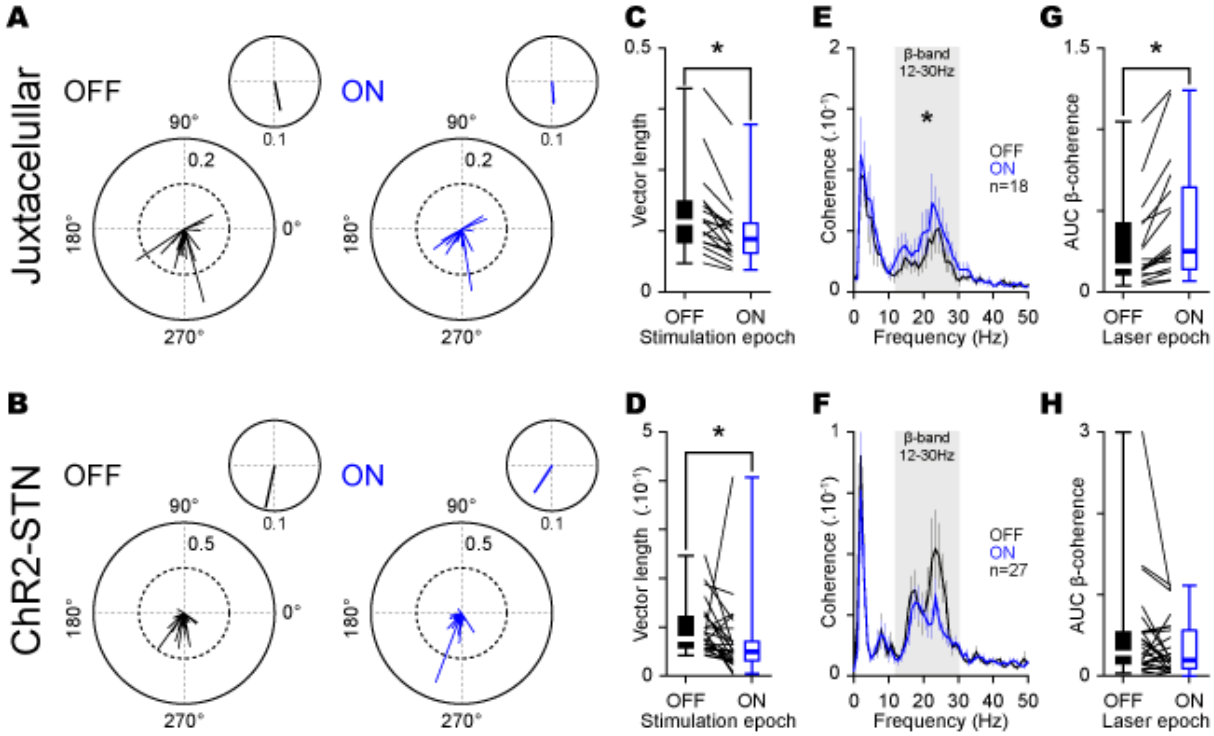

Figure S8. Effect of STN excitation on *β*-synchronization. (A, B) Individual and mean circular phase of STN neurons entrained at *β* frequency during OFF *vs.* ON juxtacellular stimulation epochs (**A**) or the OFF *vs.* ON ChR2-STN opto-excitation (**B**). **(C, D)** Box-and-whisker plots showing the change in vector lengths induced in STN neurons by the juxtacellular excitation (**C**, n=18, mean vector length OFF-juxta *vs.* ON-Juxta, 6.4 ± 0.8 $x10^{-2}$ *vs.* 4.9 ± 0.6 $x10^{-2}$, paired *t*-test, t=4.74, $p<0.001$) or the ChR2 opto-excitation (**D**, n=27, mean vector length OFF-ChR2 *vs.* ON-ChR2, 9.5 ± 1.0 $x10^{-2}$ *vs.* 7.1 ± 1.5 $x10^{-2}$, Wilcoxon signed rank test, z=-3.123, $p=0.002$). **(E, F)** Mean coherence between mCx ECoG and STN units during OFF *vs.* ON juxtacellular stimulation **(E)** or the OFF *vs.* ON ChR2-STN opto-excitation **(F)**. **(G, H)** Box-and-whisker plots comparing the *β*-band (12-30 Hz) coherence during the OFF *vs.* ON juxtacellular stimulation (**G**, n=18 neurons, AUC *β*-band coherence OFF-juxta *vs.* ON-juxta, 2.7 ± 0.6 $x10^{-1}$ *vs.* 4.0 ± 0.8 $x10^{-1}$, Wilcoxon signed rank test, z=3,724, $p<0.001$) and the OFF *vs.* ON ChR2-STN opto-excitation (**H**, n=27, AUC *β*-band coherence OFF-ChR2 *vs.* ON-ChR2, 5.1 ± 1.1 $x10^{-1}$ *vs.* 3.7 ± 0.6 $x10^{-1}$, Wilcoxon signed rank test, z=-1.802, $p=0.073$).

Figure S9

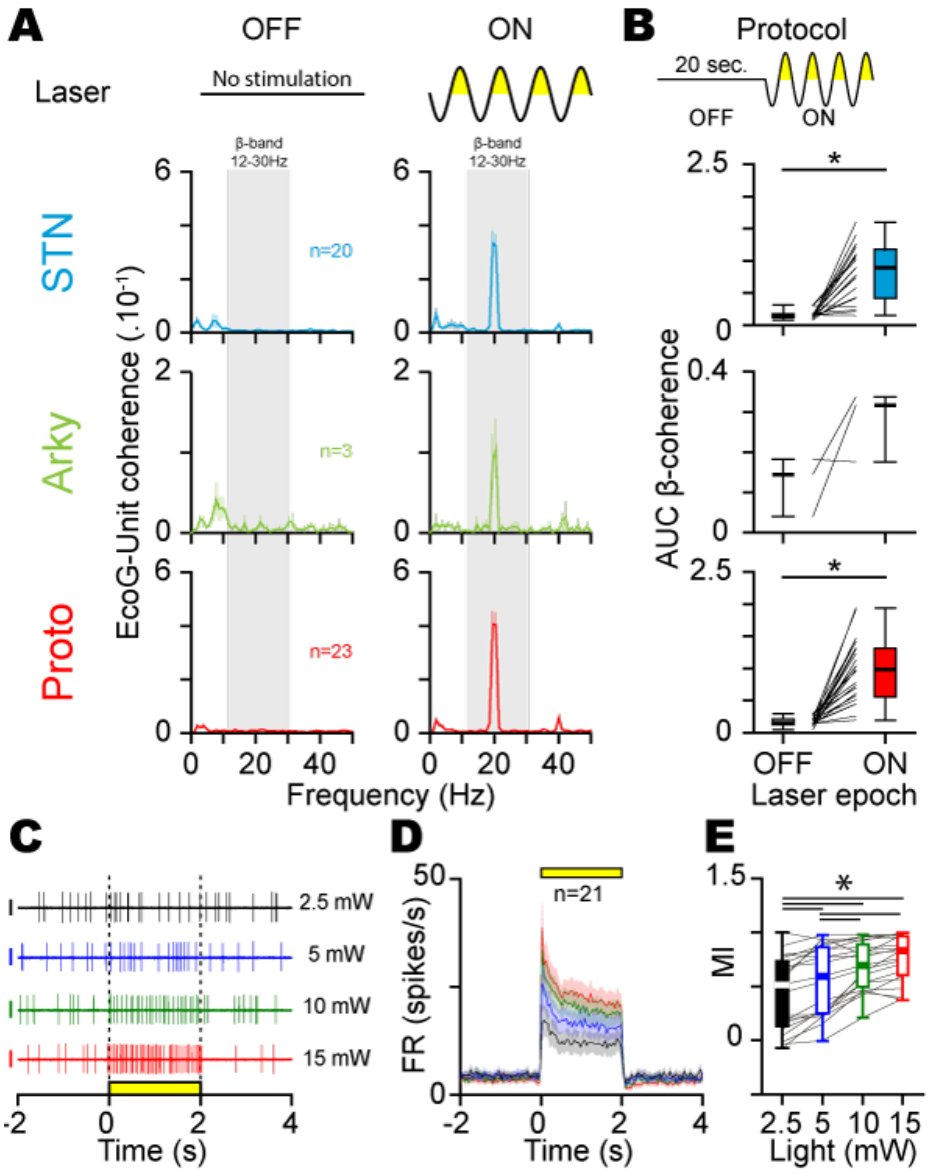

Figure S9. Optogenetic patterning of eArch3-expressing GP neurons at *β* frequency. (A) Mean Coherence calculated during the OFF *vs.* ON laser stimulation between mCx ECoG and STN (blue), or arkypallidal (black) or prototypic neurons (red). **(B)** Box-and-whisker plots comparing the *β*-coherence (12-30 Hz) OFF *vs.* ON laser stimulation for STN (blue, n=20, AUC *β*-coherence OFF *vs.* ON: 1.6 ± 0.2 x10^{-1} *vs.* 8.3 ± 1.0 x10^{-1}, paired *t*-test, t=-6.67, $p<0.001$), for arkypallidal (black, n=3, AUC *β*-coherence OFF *vs.* ON: 1.2 ± 0.4 x10^{-1} *vs.* 2.8 ± 0.5 x10^{-1}), and prototypic neuros (red, n=23, AUC *β*-coherence OFF *vs.* ON: 1.8 ± 0.1 x10^{-1} *vs.* 9.7 ± 1.0 x10^{-1}, paired *t*-test, t=-7.74, $p<0.001$). **(C)** Example of STN firing rate disinhibition induced by increasing intensity of GP opto-inhibition (scale bar: 2 mV). **(D)** Population PSTH of STN firing to increasing intensity of GP opto-inhibition (n=21 STN neurons, GP opto-inhibition at 2.5 mW in black, 5 mW in blue, 10 mW in green, and 15 mW in red). **(E)** MI of STN neurons in response to the different intensity of GP opto-inhibition (n=21, MI at 2.5 mW *vs.* 5 mW *vs.* 10 mW *vs.* 15 mW, 4.4 ± 0.7 x10^{-1} *vs.* 5.6 ± 0.7 x10^{-1} *vs.* 6.9 ± 0.5 x10^{-1} *vs.* 7.5 ± 0.5 x10^{-1}, repeated measures ANOVA, F=34.226, $p<0.001$, following by Student-Newman-Keuls post hoc test, $p<0.001$ for 2.5 mW *vs.* 5 mW, 2.5 mW *vs.* 10 mW, 2.5 mW *vs.* 15 mW, 5 mW vs. 10 mW, 5 mW *vs.* 15 mW, q= 5.0, 10.5, 13.2, 5.5 and 8.1 respectively).

Figure S10

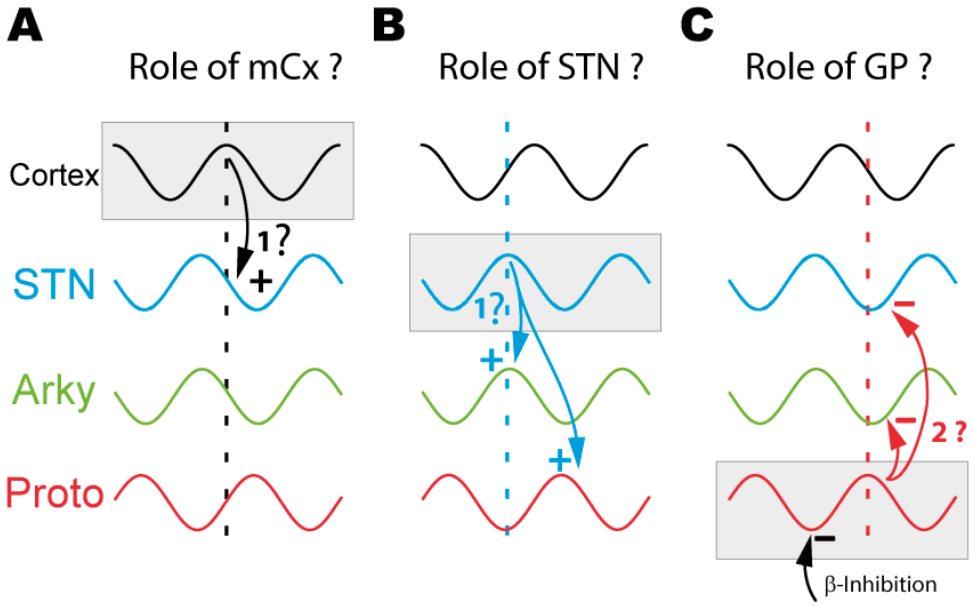

Figure S10. Circuit mechanisms driving *β*-oscillations in parkinsonism. (A-C) Schematic representation of the neuronal *β*-oscillatory activity in cortico-basal ganglia circuits illustrating the various mechanism of *β*-generation that we have tested in this work. **(A)** The motor cortex (mCx) has been proposed to drive *β*-oscillatory activity in basal ganglia circuit, possibly through the hyperdirect pathway that directly inputs excitation at the level of the STN. We demonstrate in this work that opto-inhibition of the cortex or decortication experiments have no effect on the generation/propagation of *β*-oscillations. **(B)** Another hypothesis involves the activity of STN neurons to drive *β*-oscillatory activity in globus pallidus neurons and the rest of basal ganglia. However, we show here that STN opto-inhibition and electrolytic lesion do not affect the level of *β*-oscillations expression in these circuits. In addition, reintroduction of artificial *β*-oscillations in the STN did not reproduce the functional properties of parkinsonian *β*-oscillations. **(C)** The last hypothesis we tested in this study was the contribution of GP activity to *β*-rhythm generation/propagation. Our results indicate that *β*-activity is dependent on GP neurons and driven through inhibitory mechanisms. The inhibitory drive is likely coming from striatal indirect neurons[43] that might preferentially impact onto prototypic neurons. Our work supports the view that GP neurons, and especially prototypic neurons, are critical for the orchestration and the broadcasting of *β*-rhythm to STN and cortico-basal ganglia circuits. Abbreviations: mCx: motor cortex, STN: subthalamic nucleus, GP: globus pallidus, Arky: arkypallidal neurons, Proto: prototypic neurons.

ONLINE METHODS

Animals

All Experimental procedures were performed on adult male Sprague-Dawley rats (9 to 21 weeks, Janvier Labs) in accordance with the European legislation for the protection of animals used for scientific purposes (directive 2010/63/EU). This project was also approved by the French ministry of higher education and research and the ethical committee of CNRS, Aquitaine Region (accreditation number 5012079-A). Rats were housed collectively (at least by 2) per cage under artificial conditions of light (light/dark cycle, light on at 7:00 a.m.), temperature (24°C), and humidity (45%) with food and water available ad libitum. A total number of 93 rats were used for this study of which 20 rats were excluded due to the low transduction rate of STN neurons as verified with electrophysiological recordings in STN (see 'Functional optogenetic mapping of laser effect in STN' for more details).

Stereotaxic injection of 6-hydroxydopamine

Unilateral 6-hydroxydopamine (6-OHDA) lesions were induced as previously described [10]. Briefly, rats (300-350 g) were anesthetized with isoflurane (induction/maintenance: 3-5/1.5%; Iso-vet®, Piramal healthcare), fixed on a stereotaxic frame (Unimécanique, M2e) and placed on heating blanket. An ophthalmic ointment (Liposic®, Bauch & Lomb Swiss) was used all along the surgery to prevent dehydration. Then, the rats received desipramine hydrochloride (25 mg/Kg, i.p; CAT#D3900, Sigma-Aldrich) thirty minutes before 6-OHDA injection in the right medial forebrain bundle (AP, -3.8 mm caudal to bregma; ML, 1.6 mm from midline, Paxinos and Watson 2007). This pre-treatment was used to prevent noradrenergic system lesion [89]. After subcutaneous injection of xylocaine (15 mg/Kg; AstraZeneca), skull was exposed and a craniotomy was performed to inject 2.5 µL of 6-OHDA 3% (w/v; CAT#162957, Sigma-Aldrich) solution. This latter was dissolved in saline solution containing ascorbic acid 0.1% (w/v; CAT#A4544, Sigma-Aldrich) and was injected in five points (500 nL each) separated by 250 µm vertical intervals (-7 to -8 mm from cortical surface) with glass capillary (tip diameter 35 µm; 1-5 µL Hirschmann® microcapillary pipette, CAT#Z611239, Sigma-Aldrich) connected to Picospritzer® (Parker Hannifin). At the end of surgery, 5.5% glucose solution (w/v; CAT#G8270, Sigma-Aldrich) and buprenorphine (0.05 mg/Kg; Axience) were injected subcutaneously. To assess the 6-OHDA lesion, an apomorphine challenge was performed (0.05 mg/kg, s.c.; Apokinon®, Aguettant) 14-15 days after surgery (Schwarting and Huston 1996; Mallet et al. 2008; Mallet et al. 2008). Only rats performing 80 net rotations in 20 minutes were selected in this study.

Stereotaxic injection of viral vectors

All the virus used for our optogenetic manipulations were adeno-associated virus directly purchased from a vector core (UNC vector core) and micro-injected under stereotaxic condition in control or hemi-lesioned rats using glass capillary (tip diameter 35 µm; 1-5 µL Hirschmann® microcapillary pipette, CAT#Z611239, Sigma-Aldrich) connected to a Picospritzer® pressure system (Parker Hannifin). All injections were performed under the same surgical methodology as described before. Experiments of mCx optogenetic inhibition, were achieved using an AAV2/5-CamKIIa-eArchT3-YFP viral vector (3 $x10^{12}$ viral particles/mL) injected in rats (n=13, total volume of 2 µL) injected in 4 points of the M1/M2 mCx ipsilaterally to the lesion (500 nL per injection sites at coordinates: AP, +4 mm rostral to bregma, ML, +2 and +2.8 mm from midline; AP, +3.4 mm rostral to bregma, ML, +1.8 and +2.6 from midline; DV, -1.5 mm from cortical surface, Paxinos and Watson 2007). For STN manipulations, we injected in hemi-lesioned (ipsilateral to lesion) or normal animals (right hemisphere) the viral solutions AAV2/5-CamKII-eArchT3-YFP (n=13 hemi-lesioned rats, 3 $x10^{12}$ viral particles/mL), AAV5-hSyn-eArch3-YFP (n=9 hemi-lesioned rats, 3 $x10^{12}$ viral particles/mL), or AAV2/5-CamKIIa-hChR2(H134R)-YFP (n=7 and 10 for hemi-lesioned and normal animals respectively, 6.2 $x10^{12}$ viral particles/mL) in 2 injection points in the STN (250 nL each, coordinates: AP, -3.6 and -3.9 mm caudal to bregma, ML, +2.5 mm from midline, DV, -7.5 mm from cortical surface, Paxinos and Watson 2007). For GP optogenetic inhibition, we used an AAV2/5-hSyn-eArch3-YFP (3 $x10^{12}$ viral particles/mL, 600 nL injected in 2 injections points, 300 nL each, coordinates: AP, -0.9 mm caudal to bregma, ML, +2.8 mm from midline, DV, -5.6 and 6.1 mm from cortical surface, Paxinos and Watson 2007) in GP of hemi-lesioned (n=15, ipsilateral to lesion) or control (n=18, right hemisphere) animals.

In vivo electrophysiological recording

Electrophysiological recordings and optogenetic manipulations were realized at least 4 weeks after viral transduction under urethane anaesthesia. Anaesthesia was first induced with isoflurane (3-5%; Iso-vet®, Piramal healthcare), and maintained with urethane (i.p., 1.3 g/Kg.; CAT#U2500, Sigma-Aldrich). The animals were then secured in a stereotaxic frame (Unimécanique, M2e) and placed on heating blanket. After subcutaneous injection of xylocain, skull was exposed and craniotomies were performed to unable electrophysiological recordings and optogenetic stimulation of the region of interest (same stereotaxic coordinates as above). In each rat, an electrocorticogram (ECoG) of the sensorimotor cortex were realized (AP, +4.3 mm rostral to bregma; ML, +2 mm from midline, Paxinos and Watson 2007) with a

1mm-screw juxtaposed to the dura mater (Mallet et al. 2008; Mallet et al. 2008; Mallet et al. 2012). All along the recording session, saline solution was used to prevent dehydration and anaesthesia level was frequently controlled by examination of ECoG and by testing the response to light sensory stimuli (tall pinch).

In vivo extracellular recordings were performed using glass electrodes (1-3 µm tip end, 12-20 MΩ, GC150F, WPI) filled with a chloride solution 0.5 M containing neurobiotin tracer (1-2%, w/v; CAT#SP-1120, Vector laboratories) to perform juxtacellular labelling as described below [27,91]. For GP recordings, neurons were classified as prototypic and arkypallidal neurons based on their well-known electrophysiological signature across different brain-state [27,41]. A subset of neurons (n=10) were further labelled with neurobiotin and identified according to their molecular profiles: prototypic neurons expressed the transcription factor Nkx2.1 whereas arkypallidal neurons expressed the transcription factor FoxP2. Optogenetic manipulation of the recorded neurons were performed using an opto-electrode that was homemade by gluing an optical fibers (multimode Fiber, 0.22 NA, core diameter: 105 µm, Thorlabs) 1 mm and/or 2 mm above the tip of the glass recording electrodes. This method allows extracellular recording during opto-manipulation and juxtacellular labelling. Once the opto-electrode was implanted in the recording structure, the signal was amplified 10 fold using an axoClamp 2B (in bridge mode; Molecular Devices). The recorded signal was then amplified 1000 fold and filtered using a differential AC amplifier (spike unit: 0.3 Hz-10 kHz, LFP: 0.1 Hz-10 kHz; model 1700, A-M Systems). For ECoG recording, the signal was amplified 1000 fold and filtered with the same differential AC amplifier (0.1 Hz-5 kHz). Finally, all recorded signals were digitalized at 20 kHz, by using the Power1401-3 connected to a computer equipped with Spike2 software (Cambridge Electronic Design). To facilitate the identification of STN during the recording sessions, a concentric bipolar electrode (SNEX-100, Rhodes Medical Instruments) connected to an isolated stimulator (DS3 Isolated Current Stimulator, Digitimer), was inserted in the mCx (coordinates: AP, +3.5 mm rostral to bregma, ML, +3.5 mm from midline, DV, -1.8 mm from cortical surface, Paxinos and Watson 2007). STN was identified by checking online the STN response to mCx electrical stimulation as previously described [92]. We then validated the recording location with histological control, in particular the location of the juxtacellularly-labelled neurons and the track marks left by the opto-electrode.

Functional optogenetic mapping of laser effect in STN

In order to validate the results of our STN opto-inhibition and STN opto-excitation experiments performed in 6-OHDA rats, it was critical to verify functionally that the overall level of optical control achieved in STN was acceptable. For this reason, we adopted an opto-

electrode mapping strategy that consisted of combining laser stimulation with STN extracellular recordings at multiple locations in the STN (i.e. at least 3 penetrations spaced by 150 µm in the antero-posterior or medio-lateral axis of the STN. In addition, only animals that had at least 10 STN cells opto-tested *in vivo* and presenting >60% of significantly laser-modulated cells were kept for further analysis. Using these criteria, hemi-lesioned animals with poor STN optogenetic control were excluded from the study, that is: 9 out of 13 rats injected with AAV5-CamKII-eArch3-EYFP; 5 out of 9 injected with AAV5-hSyn-eArch3-EYFP; and 2 out of 7 injected with AAV5-CamKII-ChR2-EYFP. The level of STN optical control was also verified/quantified in normal animals injected with an AAV5-CamKII-ChR2-EYFP (4 out of 10 excluded) or with the AAV5-CamKII-eArchT3.0-EYFP (none excluded out of 4).

Optogenetic stimulation

To apply optogenetic stimulation, we implanted optical fibers (multimode Fiber, 0.22 NA, core diameter: 105 µm, Thorlabs) into the GP (coordinates: AP, -0.9 mm caudal to bregma, ML, +2.8 mm from midline, DV, -5.6 and 6.1 mm from cortical surface, Paxinos and Watson 2007) or STN (coordinates: AP, -3.7 mm to bregma, ML, +2.5 mm from midline, DV, -7.0 mm from cortical surface, Paxinos and Watson 2007) or mCx. Note that for mCx inhibition, 2 optic fibers were implanted to maximize the volume of cortical inhibition (coordinates: AP, +4 mm rostral to bregma, ML, +2.2 mm from midline; AP, +3.4 mm rostral to bregma, ML, +2.2 mm from midline; DV, -1.0 mm from cortical surface, Paxinos and Watson 2007). The power at the tip of the optics fibers was always measured with a power meter (PM100D, Thorlabs) right before insertion in brain tissue. Two optogenetic stimulation protocols were used in this study. The first one consisted of 2 s of continuous yellow or blue light (15 or 2.5 mW at the tip of optical fiber respectively) every 10 s. The 2 s preceding the light pulse was used as baseline (OFF period) to compare the effect of the 2 s of optogenetic manipulation (ON epoch). Only recordings that contained a minimum of 30 laser stimulations (and at least 60 s during OFF and ON epochs) were kept for analyses to quantify the effect of the optogenetic inhibitions on β-synchronization (phase locking, ECoG power and coherence). For each animal, the best β-oscillations recording was determined based on the highest peak in the β-AUC (12-30 Hz) power spectrum calculation. The effect of our optogenetic manipulations on the neuronal firing rate measured in STN and GP neurons (in hemi-lesioned and control animals) were determined using at least 10 laser stimulations. To reintroduce abnormal β-synchronization in control animal, we used a different protocol that consisted of 20 s of sinusoidal yellow or blue light stimulation (15 or 2.5 mW at the tip of optical fiber,

respectively). Only the positive part of the sinusoid drove laser activation. The baseline OFF epoch consisted of the 20 s before light stimulation and was compared to the ON epoch that contains 20 s of sinusoidal stimulation. Only recording with at least 3 sinusoidal protocols (60 s) were included in this study. The laser diode (Errol laser) was controlled by an analogic signals sent by a Power1401-3 (Cambridge Electronic Design) and controlled with the Spike2 software (Cambridge Electronic Design).

Decortication experiments and STN electrolytic lesion

To test the importance of other cortical area in the generation mechanism of β-oscillations we performed large-scale decortication experiments. Removal of the temporal and frontal bones exposed most of the dorsal cortical surface. We removed the cortical tissue using an electrosurgical cautery (BC 50D, Anhui Yingte Electronic) and the depth of the lesion was assesses based on the visual inspection of the corpus callosum. As shown in supplementary Figure S2, this approach allowed to lesion a broad cortical volume including the M1, M2, S1 and a large part of the S2 cortex. In these experiments, brain state activity was monitored through an ECoG recorded above mCx on the contralateral side of the lesion and combined with GP LFP recording (ipsilateral to lesion) using 32-channel silicon probe microelectrodes (Cambridge Neurotech, GB) in anaesthetized hemi-lesioned rats (n=3).

To further test the contribution of STN in generating β-oscillations, we performed an electrolytic lesion of the STN in anaesthetized hemi-lesioned rats (n=3). We first performed electrophysiological recordings to map the exact stereotaxic location and depth of the STN. We then lowered a concentric bipolar electrode (SNEX-100, Rhodes Medical Instruments) and located the tip of the electrode at the bottom of the STN. The electrode was connected to an isolated stimulator (DS3 Isolated Current Stimulator, Digitimer) and an electrolytic lesion was performed by applying a continuous current (3 mA during 20 s) in two stereotaxic coordinates separated by 300 µm in the rostro-caudal axis. Ipsilateral ECoG recording was performed before and after STN lesion.

Juxtacellular stimulation

In this study, we performed juxtacellular labelling to identify the location/cell-type of the recorded unit in STN or in GP. Briefly, the recorded unit was stimulated by a current pulse of 250 ms long (50 % duty cycle, 1-10 nA) sent through the recording electrode by axoClamp 2B (in bridge mode; Molecular Devices). Only recording with at least 250 stimulations were included in this study.

Data processing and analysis

We performed simultaneous recording of the mCx ECoG and STN unit activity at a sampling rate of 20kHz during epoch containing *β*-synchronization. All data processing (spike sorting and ECoG filtering) were realized offline with Spike2 software (Cambridge Electronic Design). The ECoG signal was high-pass filtered at 0.5Hz (DC remove) and low-pass filtered at 500 Hz following by a down-sampling at the same frequency (to avoid aliasing effect) for further field analysis. The frequency resolution was set at around 1 Hz (FFT size = 500/512 Hz) to analyse the root mean square ECoG power spectrum or to calculate the coherence between spike train and ECoG (using "coher" script, freely available on CED website). For generating perievent spectrograms, we computed in Matlab® R2016a (MathWorks, Natick, MA, USA) using the ft_freqanalysis function (time/frequency slide windows: 50 ms /0.071 Hz, cycle number: 7) of the Fieldtrip toolbox [93]. Peri-stimulus time histograms or PSTH (width: 6 s, offset: 2 s, bin size: 50 ms) of each spike trains were generated using spike2 and a custom Matlab® script. Both frequency and count PSTH were generated for each spike train to evaluate the effect of the optogenetic manipulations. A response was classified as statistically significant if the spike count values of 3 consecutive bins within the first 400 ms of light pulse delivery were < -2SD (inhibitory response) or > 2SD (excitatory response). SD was measured during OFF epoch. We also analysed in spike2 the frequency of each spike train during OFF and ON epoch. This allowed us to calculate the modulatory index or MI [94] for evaluating the frequency increasing induced by our manipulations. MI was calculated as follow: (frequency ON - frequency OFF) / (frequency ON + frequency OFF).

To generate the linear phase histograms in spike2 (bin size: 10°), we detected the peak of *β*-oscillations in the band-pass filtered (12-30 Hz) ECoG using a threshold detection as previously described (Mallet et al. 2008; Mallet et al. 2012). The linear phase histograms were then transferred to Matlab® for further analysis using circular statistics toolbox [95]. To determine if a spike activity was significantly modulated by the *β*-oscillations measured in the ECoG, we performed the Rayleigh test for circular uniformity using the 'circ_rtest' function which evaluates if the spike unit activity is uniformly distributed across the ECoG *β*-oscillation cycles (H0, $p>0.05$). If H0 was rejected, neuron was considered as significantly entrained by *β*-oscillations. The mean angle and vector length for each spike train were also measured by using the 'circ_mean' and 'circ_r' function, respectively. Finally, the mean angles of entrained neurons were compared (OFF *vs.* ON epoch or between groups) by using the Watson-Williams F test ('circ_wwtest' function, circular statistics toolbox).

Random spike removing in mCx experiment

Our mCx optogenetic inhibition was associated with a reduction in the firing rate of STN neurons and a consequent decrease in the coherence value measured between STN spike and ECoG reduction in the functional connectivity. To determine the influence of change in firing rate on the spike-ECoG coherence value we performed random spike removal on our STN spike timestamps using the 'randsample' Matlab® function. We analysed the effect of a 20% or 50% decrease in STN firing rate and performed coherence analysis in Spike2 as previously described.

Effect of optogenetic stimulation across *β*-oscillations power distribution

To analyse the effect of the optogenetic stimulation across the *β*-power distribution, we compared the root mean square power of every individual *β* oscillations period as measured through the area under the curve (AUC) within the 12-30 Hz frequency band for each stimulation epoch (OFF laser *vs.* ON laser) for each neuron. The *β*-AUC was calculated in Matlab® through an interpolation method ('interp1' function) of the power spectrum in the 12 to 30 Hz frequency band. A *β*-AUC difference (*β*-AUC above interpolated line) - (*β*-AUC below interpolated line) was calculated for every 2 s long stimulation epoch (OFF and ON laser stimulation). Finally, the cumulative distribution was computed with the 'cdfplot' function (Matlab®).

Beta bursts detection

The *β* bursts were extracted from the ECoG signal recorded above the mCx and according to a threshold detection method previously published [96]. The signal was first down sampled at 500 Hz and band-pass filtered in the β-band (see Data processing and analysis). The filtered EcoG signal was then imported into Matlab and the envelope of the *β* signal was calculated using the hilbert() function. The signal was defined as a beta burst if: 1/ the amplitude of the envelope exceeding the 75th percentile threshold of the analytic signal measured during the entire recording, and 2/ the duration of the burst was longer than 50 ms. Finally, the duration and the number of *β*-bursts were averaged accordingly to the 3 laser epochs (i.e. Before, OFF and ON) and statistically compared.

Tissue processing and histological control

At this end of recording day, the rats were sacrificed with an overdose of pentobarbital sodium (150 mg/Kg, i.p.; Axience). An intracardiac perfusion (PBS 0.01mM following by formaldehyde 4%) was then performed for further histological validations. The brain was kept overnight in a solution of PBS 0.01 mM / formaldehyde 4% (v/v; CAT#20909.330, VWR) and then cut in 50 µm slices with a vibratome (VT1000, Leica Microsystemes). To reveal the juxtacellularly labelled neurons, the slices were incubated overnight in a solution of PBS 0.01

mM / Triton™ X100 0.3% (v/v; CAT#T9284, Sigma-Aldrich) containing streptavidine-CY3 Zymax (1/1000, v/v; CAT#438315, Life Technologies). The slices were then washed in PBS 0.01 mM before mounting onto slides in vectashield medium (CAT#H-1000, Vector laboratories). Additional staining was performed through indirect immunofluorescence staining using primary and fluorescent secondary antibodies. For all immunostainings, the slices were incubated overnight in a solution of PBS 0.01mM / Triton™ X100 0.3% (v/v) containing the primary antibody. The slices were then washed 3 times in PBS 0.01 mM, incubated 4h in a solution of PBS 0.01 mM / Triton™ X100 0.3% (v/v) containing the secondary antibody, washed again in PBS 0.01 mM and mounted onto slides in vectashield medium (CAT#H-1000, Vector laboratories). The primary antibodies used in this study were: chicken anti-YFP (1/1000, v/v; CAT#GFP-1020, Avès labs), rabbit anti-Nkx2.1 (or anti-TTF-1, prototypic neuron labelling, 1/500, v/v; CAT#H-190, Santa Cruz) and goat anti-FoxP2 (arkypallidal neuron labelling, 1/500, v/v; CAT#N-16, Santa Cruz). The secondary antibodies used were: Alexa Fluor® 488 donkey anti-chicken (1/500, v/v; CAT#703-545-155, Jackson ImmunoResearch), CY™5-conjugated donkey anti-rabbit (1/500, v/v; CAT#711-175-152, Jackson ImmunoResearch), and Brilliant Violet™421-conjugated donkey anti-goat (1/500, v/v; CAT#705-675-147, Jackson ImmunoResearch). The images were acquired with a fluorescence microscope (Axio Imager 2, Zeiss) or a confocal microscope (Leica, SP8) and were analysed with Fiji (ImageJ 1.52) [97]. To determine if our opto-mapping recordings applied to STN opto-inhibition experiments in parkinsonian rats accurately capture the level of STN infection (**Figure S3A, B**), we performed an histological quantification of the effectiveness and spread of virus infection in the STN. To do so, we determined the intensity of STN fluorescence in the EYFP channel using Region of Interest (ROI) measures in Fiji. Briefly, we mounted serial brain sections spaced by 300 µm and containing STN sagittal slices at different medio-lateral coordinate (i.e. 2.9/2.6/2.3/2 mm from the midline). For each slices, the value of ROI was normalized according to the background labelling in a region devoid of EYFP signal and taken just below the STN region. For each rat, we averaged the different STN ROI values and correlated this measure to the percentage of opto-inhibition as determined by our opto-mapping strategy.

Statistical Analysis

The statistical analyses were performed using SigmaPlot 12 (Systat Software). For independent samples, we applied the normality (Shapiro-Wilk test) and equal variance tests. A *t*-test was used if the distributions were normal and the group variances were equal. Otherwise, the Mann-Whitney signed rank test was used. In a same way, Kruskal-Wallis one

way ANOVA was used instead of one way ANOVA, when normality distributions and variance homogeneity were not verified. ANOVA was followed by Student-Newman-Keuls post hoc test. For dependant sample, the paired *t*-test was used excepts if the normality distribution test failed (Shapiro-Wilk test, $p<0.05$). In the latter case, the Wilcoxon signed rank test was used. In same way, Friedman repeated measures ANOVA on ranks was used instead of one way repeated measure ANOVA, when normality distribution was not verified. ANOVA repeated measure was followed by Holm-Sidak (parametric) or Dunn's (non-parametric) post hoc test.

Data and Code Availability

The data that support the findings and the code for the analysis are available from the corresponding author upon request.

References

1. Ainsworth, M. *et al.* Rates and Rhythms: A Synergistic View of Frequency and Temporal Coding in Neuronal Networks. *Neuron* **75**, 572–583 (2012).

2. Schoffelen, J. M., Oostenveld, R. & Fries, P. Neuronal coherence as a mechanism of effective corticospinal interaction. *Science (80-.).* **308**, 111–113 (2005).

3. Uhlhaas, P. J. & Singer, W. Neural Synchrony in Brain Disorders: Relevance for Cognitive Dysfunctions and Pathophysiology. *Neuron* **52**, 155–168 (2006).

4. DeLong, M. R. Primate models of movement disorders of basal ganglia origin. *Trends Neurosci.* **13**, 281–285 (1990).

5. Albin, R. L., Young, A. B. & Penney, J. B. The functional anatomy of basal ganglia disorders. *Trends Neurosci.* **12**, 366–75 (1989).

6. Hutchison, W. D. Neuronal Oscillations in the Basal Ganglia and Movement Disorders: Evidence from Whole Animal and Human Recordings. *J. Neurosci.* **24**, 9240–9243 (2004).

7. Raz, A., Vaadia, E. & Bergman, H. Firing patterns and correlations of spontaneous discharge of pallidal neurons in the normal and the tremulous 1-methyl-4-phenyl-1,2,3,6-tetrahydropyridine vervet model of parkinsonism. *J. Neurosci.* **20**, 8559–71 (2000).

8. Bergman, H. *et al.* Physiological aspects of information processing in the basal ganglia of normal and parkinsonian primates. *Trends Neurosci.* **21**, 32–38 (1998).

9. Plotkin, J. L. & Goldberg, J. A. Thinking Outside the Box (and Arrow): Current Themes in Striatal Dysfunction in Movement Disorders. *Neurosci.* **25**, 359–379 (2019).

10. Mallet, N., Ballion, B., Le Moine, C. & Gonon, F. Cortical inputs and GABA interneurons imbalance projection neurons in the striatum of parkinsonian rats. *J. Neurosci.* **26**, 3875–3884 (2006).

11. Parker, J. G. *et al.* Diametric neural ensemble dynamics in parkinsonian and dyskinetic states. *Nature* **557**, 177–182 (2018).

12. Kravitz, A. V *et al.* Regulation of parkinsonian motor behaviours by optogenetic control of basal ganglia circuitry. *Nature* **466**, 622–6 (2010).

13. Sharott, A. *et al.* Activity Parameters of Subthalamic Nucleus Neurons Selectively Predict Motor Symptom Severity in Parkinson's Disease. *J. Neurosci.* **34**, 6273–6285 (2014).

14. Sanders, T. H., Clements, M. A. & Wichmann, T. Parkinsonism-related features of neuronal discharge in primates. *J. Neurophysiol.* **110**, 720–731 (2013).

15. Hutchison, W. D. *et al.* Neuronal oscillations in the basal ganglia and movement disorders: evidence from whole animal and human recordings. *J. Neurosci.* **24**, 9240–3 (2004).

16. Stein, E. & Bar-Gad, I. B Oscillations in the Cortico-Basal Ganglia Loop During Parkinsonism. *Exp. Neurol.* **245**, 52–9 (2013).

17. Hammond, C., Bergman, H. & Brown, P. Pathological synchronization in Parkinson's disease: networks, models and treatments. *Trends Neurosci.* **30**, 357–364 (2007).

18. Neumann, W.-J. *et al.* Subthalamic synchronized oscillatory activity correlates with motor impairment in patients with Parkinson's disease. *Mov. Disord.* **31**, 1748–1751 (2016).

19. Little, S., Pogosyan, A., Kuhn, A. A. & Brown, P. Beta band stability over time correlates with Parkinsonian rigidity and bradykinesia. *Exp. Neurol.* **236**, 383–388

(2012).

20. Ermentrout, B., Pascal, M. & Gutkin, B. The effects of spike frequency adaptation and negative feedback on the synchronization of neural oscillators. *Neural Comput.* **13**, 1285–1310 (2001).

21. Pavlides, A., Hogan, S. J. & Bogacz, R. Computational Models Describing Possible Mechanisms for Generation of Excessive Beta Oscillations in Parkinson's Disease. *PLOS Comput. Biol.* **11**, e1004609 (2015).

22. Rubin, J. E. Computational models of basal ganglia dysfunction: the dynamics is in the details. *Curr. Opin. Neurobiol.* **46**, 127–135 (2017).

23. Shouno, O., Tachibana, Y., Nambu, A. & Doya, K. Computational Model of Recurrent Subthalamo-Pallidal Circuit for Generation of Parkinsonian Oscillations. *Front. Neuroanat.* **11**, 1–15 (2017).

24. Plenz, D. & Kital, S. T. A basal ganglia pacemaker formed by the subthalamic nucleus and external globus pallidus. *Nature* **400**, 677–682 (1999).

25. Bevan, M. Move to the rhythm: oscillations in the subthalamic nucleus–external globus pallidus network. *Trends Neurosci.* **25**, 525–531 (2002).

26. Mallet, N. *et al.* Parkinsonian beta oscillations in the external globus pallidus and their relationship with subthalamic nucleus activity. *J. Neurosci.* **28**, 14245–14258 (2008).

27. Mallet, N. *et al.* Dichotomous organization of the external globus pallidus. *Neuron* **74**, 1075–86 (2012).

28. Brittain, J. S. & Brown, P. Oscillations and the basal ganglia: Motor control and beyond. *Neuroimage* **85**, 637–647 (2014).

29. McCarthy, M. M. *et al.* Striatal origin of the pathologic beta oscillations in Parkinson's disease. *Proc. Natl. Acad. Sci.* **108**, 11620–11625 (2011).

30. Leblois, A., Boraud, T., Meissner, W., Bergman, H. & Hansel, D. Competition between feedback loops underlies normal and pathological dynamics in the basal ganglia. *J. Neurosci.* **26**, 3567–83 (2006).

31. Corbit, V. L. *et al.* Pallidostriatal Projections Promote Beta Oscillations in a

Dopamine-Depleted Biophysical Network Model. *J. Neurosci.* **36**, 5556–5571 (2016).

32. Steriade, M. Grouping of brain rhythms in corticothalamic systems. *Neuroscience* **137**, 1087–1106 (2006).

33. Jones, E. G. Synchrony in the interconnected circuitry of the thalamus and cerebral cortex. *Ann. N. Y. Acad. Sci.* **1157**, 10–23 (2009).

34. Li, Q. *et al.* Therapeutic deep brain stimulation in Parkinsonian rats directly influences motor cortex. *Neuron* **76**, 1030–41 (2012).

35. Nambu, A. & Tachibana, Y. Mechanism of parkinsonian neuronal oscillations in the primate basal ganglia: some considerations based on our recent work. *Front. Syst. Neurosci.* **8**, 74 (2014).

36. Mallet, N. *et al.* Disrupted dopamine transmission and the emergence of exaggerated beta oscillations in subthalamic nucleus and cerebral cortex. *J. Neurosci.* **28**, 4795–4806 (2008).

37. Lepage, K. Q., Kramer, M. A. & Eden, U. T. The dependence of spike field coherence on expected intensity. *Neural Comput.* **23**, 2209–2241 (2011).

38. Deffains, M. *et al.* Subthalamic, not striatal, activity correlates with basal ganglia downstream activity in normal and parkinsonian monkeys. *Elife* **5**, 1–38 (2016).

39. Gradinaru, V., Mogri, M., Thompson, K. R., Henderson, J. M. & Deisseroth, K. Optical Deconstruction of Parkinsonian Neural Circuitry. *Science (80-.).* **324**, 354–359 (2009).

40. Kita, H. & Kitai, S. T. Intracellular study of rat globus pallidus neurons: membrane properties and responses to neostriatal, subthalamic and nigral stimulation. *Brain Res.* **564**, 296–305 (1991).

41. Mallet, N. *et al.* Arkypallidal Cells Send a Stop Signal to Striatum. *Neuron* **89**, 308–316 (2016).

42. Abdi, A. *et al.* Prototypic and Arkypallidal Neurons in the Dopamine-Intact External Globus Pallidus. *J. Neurosci.* **35**, 6667–6688 (2015).

43. Sharott, A., Vinciati, F., Nakamura, K. C. & Magill, P. J. A population of indirect

pathway striatal projection neurons is selectively entrained to parkinsonian beta oscillations. *J. Neurosci.* **37**, 0658–17 (2017).

44. Brown, P. Abnormal oscillatory synchronisation in the motor system leads to impaired movement. *Curr. Opin. Neurobiol.* **17**, 656–664 (2007).

45. Fogelson, N. *et al.* Different functional loops between cerebral cortex and the subthalmic area in parkinson's disease. *Cereb. Cortex* **16**, 64–75 (2006).

46. Williams, D. *et al.* Dopamine-dependent changes in the functional connectivity between basal ganglia and cerebral cortex in humans. *Brain* **125**, 1558–69 (2002).

47. Litvak, V. *et al.* Resting oscillatory cortico-subthalamic connectivity in patients with Parkinson's disease. *Brain* **134**, 359–374 (2011).

48. Lalo, E. *et al.* Patterns of Bidirectional Communication between Cortex and Basal Ganglia during Movement in Patients with Parkinson Disease. *J. Neurosci.* **28**, 3008–3016 (2008).

49. Sharott, A., Magill, P. J., Bolam, J. P. & Brown, P. Directional analysis of coherent oscillatory field potentials in the cerebral cortex and basal ganglia of the rat. *J. Physiol.* **562**, 951–63 (2005).

50. Surmeier, D. J., Mercer, J. N. & Chan, C. S. Autonomous pacemakers in the basal ganglia: who needs excitatory synapses anyway? *Curr. Opin. Neurobiol.* **15**, 312–8 (2005).

51. Chu, H.-Y., McIver, E. L., Kovaleski, R. F., Atherton, J. F. & Bevan, M. D. Loss of Hyperdirect Pathway Cortico-Subthalamic Inputs Following Degeneration of Midbrain Dopamine Neurons. *Neuron* **95**, 1306-1318.e5 (2017).

52. Mathai, A. *et al.* Reduced cortical innervation of the subthalamic nucleus in MPTP-treated parkinsonian monkeys. *Brain* **138**, 946–962 (2015).

53. Sanders, T. H. & Jaeger, D. Optogenetic stimulation of cortico-subthalamic projections is sufficient to ameliorate bradykinesia in 6-ohda lesioned mice. *Neurobiol. Dis.* **95**, 225–237 (2016).

54. Sharott, A. *et al.* Dopamine depletion increases the power and coherence of β-

oscillations in the cerebral cortex and subthalamic nucleus of the awake rat. *Eur. J. Neurosci.* **21**, 1413–1422 (2005).

55. Leventhal, D. K. *et al.* Basal Ganglia Beta Oscillations Accompany Cue Utilization. *Neuron* **73**, 523–536 (2012).

56. Rubino, D., Robbins, K. A. & Hatsopoulos, N. G. Propagating waves mediate information transfer in the motor cortex. *Nat. Neurosci.* **9**, 1549–1557 (2006).

57. Gilbertson, T. *et al.* Existing motor state is favored at the expense of new movement during 13-35 Hz oscillatory synchrony in the human corticospinal system. *J. Neurosci.* **25**, 7771–9 (2005).

58. Engel, A. K. & Fries, P. Beta-band oscillations-signalling the status quo? *Curr. Opin. Neurobiol.* **20**, 156–165 (2010).

59. Mirzaei, A. *et al.* Sensorimotor Processing in the Basal Ganglia Leads to Transient Beta Oscillations during Behavior. *J. Neurosci.* **37**, 11220–11232 (2017).

60. Deffains, M., Iskhakova, L., Katabi, S., Israel, Z. & Bergman, H. Longer β oscillatory episodes reliably identify pathological subthalamic activity in Parkinsonism. *Mov. Disord.* **33**, 1609–1618 (2018).

61. Bergman, H., Wichmann, T., Karmon, B. & DeLong, M. R. The primate subthalamic nucleus. II. Neuronal activity in the MPTP model of parkinsonism. *J. Neurophysiol.* **72**, 507–20 (1994).

62. Shink, E., Bevan, M. D., Bolam, J. P. & Smith, Y. The subthalamic nucleus and the external pallidum: two tightly interconnected structures that control the output of the basal ganglia in the monkey. *Neuroscience* **73**, 335–357 (1996).

63. Baufreton, J., Atherton, J. F., Surmeier, D. J. & Bevan, M. D. Enhancement of excitatory synaptic integration by GABAergic inhibition in the subthalamic nucleus. *J. Neurosci.* **25**, 8505–17 (2005).

64. Bevan, M. D., Wilson, C. J., Bolam, J. P. & Magill, P. J. Equilibrium potential of GABA(A) current and implications for rebound burst firing in rat subthalamic neurons in vitro. *J. Neurophysiol.* **83**, 3169–72 (2000).

65. Gittis, A. H. *et al.* Rapid target-specific remodeling of fast-spiking inhibitory circuits after loss of dopamine. *Neuron* **71**, 858–868 (2011).

66. Chu, H.-Y., Atherton, J. F., Wokosin, D., Surmeier, D. J. & Bevan, M. D. Heterosynaptic Regulation of External Globus Pallidus Inputs to the Subthalamic Nucleus by the Motor Cortex. *Neuron* 1–13 (2015). doi:10.1016/j.neuron.2014.12.022

67. Tanimura, A., Du, Y., Kondapalli, J., Wokosin, D. L. & Surmeier, D. J. Cholinergic Interneurons Amplify Thalamostriatal Excitation of Striatal Indirect Pathway Neurons in Parkinson's Disease Models. *Neuron* **101**, 444-458.e6 (2019).

68. Paz, J. T., Deniau, J.-M. & Charpier, S. Rhythmic bursting in the cortico-subthalamo-pallidal network during spontaneous genetically determined spike and wave discharges. *J. Neurosci.* **25**, 2092–101 (2005).

69. Alexander, G. E. & Crutcher, M. D. Functional architecture of basal ganglia circuits: neural substrates of parallel processing. *Trends Neurosci.* **13**, 266–271 (1990).

70. Kita, H. Globus pallidus external segment. *Prog. Brain Res.* **160**, 111–33 (2007).

71. Gittis, A. H. *et al.* New Roles for the External Globus Pallidus in Basal Ganglia Circuits and Behavior. *J. Neurosci.* **34**, 15178–15183 (2014).

72. Mastro, K. J. *et al.* Cell-specific pallidal intervention induces long-lasting motor recovery in dopamine-depleted mice. *Nat. Neurosci.* **20**, 815–823 (2017).

73. Mastro, K. J., Bouchard, R. S., Holt, H. a K. & Gittis, A. H. Transgenic mouse lines subdivide external segment of the globus pallidus (GPe) neurons and reveal distinct GPe output pathways. *J. Neurosci.* **34**, 2087–99 (2014).

74. Fujiyama, F. *et al.* A single-neuron tracing study of arkypallidal and prototypic neurons in healthy rats. *Brain Struct. Funct.* **221**, 4733–4740 (2016).

75. Fan, K. Y., Baufreton, J., Surmeier, D. J., Chan, C. S. & Bevan, M. D. Proliferation of external globus pallidus-subthalamic nucleus synapses following degeneration of midbrain dopamine neurons. *J. Neurosci.* **32**, 13718–28 (2012).

76. Oorschot, D. E. Total number of neurons in the neostriatal, pallidal, subthalamic, and substantia nigral nuclei of the rat basal ganglia: A stereological study using the

cavalieri and optical disector methods. *J. Comp. Neurol.* **366**, 580–599 (1996).

77. Koshimizu, Y., Fujiyama, F., Nakamura, K. C., Furuta, T. & Kaneko, T. Quantitative analysis of axon bouton distribution of subthalamic nucleus neurons in the rat by single neuron visualization with a viral vector. *J. Comp. Neurol.* **521**, 2125–46 (2013).

78. Fujiyama, F. *et al.* Exclusive and common targets of neostriatofugal projections of rat striosome neurons: A single neuron-tracing study using a viral vector. *Eur. J. Neurosci.* **33**, 668–677 (2011).

79. Kumar, A., Cardanobile, S., Rotter, S. & Aertsen, A. The Role of Inhibition in Generating and Controlling Parkinson's Disease Oscillations in the Basal Ganglia. *Front. Syst. Neurosci.* **5**, 1–14 (2011).

80. Terman, D., Rubin, J. E., Yew, a C. & Wilson, C. J. Activity patterns in a model for the subthalamopallidal network of the basal ganglia. *J. Neurosci.* **22**, 2963–2976 (2002).

81. Bar-Gad, I., Heimer, G., Ritov, Y. & Bergman, H. Functional Correlations between Neighboring Neurons in the Primate Globus Pallidus Are Weak or Nonexistent. *J. Neurosci.* **23**, 4012–4016 (2003).

82. Edgerton, J. R. & Jaeger, D. Dendritic Sodium Channels Promote Active Decorrelation and Reduce Phase Locking to Parkinsonian Input Oscillations in Model Globus Pallidus Neurons. *J. Neurosci.* **31**, 10919–10936 (2011).

83. Bevan, M. D., Booth, P. A. C., Eaton, S. A. & Bolam, J. P. Selective Innervation of Neostriatal Interneurons by a Subclass of Neuron in the Globus Pallidus of the Rat. *J. Neurosci.* **18**, 9438–9452 (1998).

84. Brazhnik, E., McCoy, A. J., Novikov, N., Hatch, C. E. & Walters, J. R. Ventral Medial Thalamic Nucleus Promotes Synchronization of Increased High Beta Oscillatory Activity in the Basal Ganglia-Thalamocortical Network of the Hemiparkinsonian Rat. *J. Neurosci.* **36**, 4196–4208 (2016).

85. Tachibana, Y., Iwamuro, H., Kita, H., Takada, M. & Nambu, A. Subthalamo-pallidal interactions underlying parkinsonian neuronal oscillations in the primate basal ganglia. *Eur. J. Neurosci.* **34**, 1470–84 (2011).

86. Beck, G., Singh, A. & Papa, S. M. Dysregulation of striatal projection neurons in Parkinson's disease. *J. Neural Transm.* **125**, 449–460 (2018).

87. Liang, L., DeLong, M. R. & Papa, S. M. Inversion of Dopamine Responses in Striatal Medium Spiny Neurons and Involuntary Movements. *J. Neurosci.* **28**, 7537–7547 (2008).

88. Paxinos, G. & Watson, C. The Rat Brain in Stereotaxic Coordinates Sixth Edition. *Elsevier Acad. Press* **170**, 547–612 (2007).

89. Schwarting, R. K. W. & Huston, J. P. The unilateral 6-hydroxydopamine lesion model in behavioral brain research. Analysis of functional deficits, recovery and treatments. *Prog. Neurobiol.* **50**, 275–331 (1996).

90. Bastide, M. F. *et al.* Inhibiting Lateral Habenula Improves L-DOPA-induced Dyskinesia. *Biol. Psychiatry* **79**, 345–353 (2014).

91. Pinault, D. A novel single-cell staining procedure performed in vivo under electrophysiological control: Morpho-functional features of juxtacellularly labeled thalamic cells and other central neurons with biocytin or Neurobiotin. *J. Neurosci. Methods* **65**, 113–136 (1996).

92. Magill, P. J., Sharott, A., Bevan, M. D., Brown, P. & Bolam, J. P. Synchronous unit activity and local field potentials evoked in the subthalamic nucleus by cortical stimulation. *J. Neurophysiol.* **92**, 700–714 (2004).

93. Oostenveld, R., Fries, P., Maris, E. & Schoffelen, J. M. FieldTrip: Open source software for advanced analysis of MEG, EEG, and invasive electrophysiological data. *Comput. Intell. Neurosci.* **2011**, (2011).

94. Oldenburg, I. A. & Sabatini, B. L. Antagonistic but Not Symmetric Regulation of Primary Motor Cortex by Basal Ganglia Direct and Indirect Pathways. *Neuron* **86**, 1174–1181 (2015).

95. Berens, P. CircStat : A MATLAB Toolbox for Circular Statistics. *J. Stat. Softw.* **31**, 1–21 (2009).

96. Cagnan, H. *et al.* Temporal evolution of beta bursts in the parkinsonian cortical and basal ganglia network. *Proc. Natl. Acad. Sci.* **116**, 16095–16104 (2019).

97. Schindelin, J. *et al.* Fiji: an open-source platform for biological-image analysis. *Nat. Methods* **9**, 676–682 (2012).